Validation of plasticity and damage model for aluminium 6014-T6

Primc, Davide

Master's thesis / Diplomski rad

2024

University of Zagreb
Faculty of Mechanical Engineering and Naval Architecture

Validation of Plasticity and Damage Model for Aluminium 6014-T6

Master's Thesis

Davide Primc

Zagreb, 2024.

University of Zagreb
Faculty of Mechanical Engineering and Naval Architecture

Validation of Plasticity and Damage Model for Aluminium 6014-T6

MASTER'S THESIS

Mentor:
Dr. sc. Tomislav Lesičar

Davide Primc

ZAGREB, 2024.

Statement

Hereby I declare that I have prepared this thesis independently, using the knowledge acquired during my studies and the cited literature. I would also like to point out that the work covered by this thesis has been supported by AVL-AST d.o.o. office in Zagreb, an official subsidiary of AVL GmbH with headquarters in Graz.

I would like to take this opportunity to thank the PTE department manager of the Zagreb office Mr. Nikola Naranča, for giving me the opportunity to work on this R&D project. Many thanks go to Mr. Roman Baranja and Mr. Richard Tichy for all their help in preparation of this master thesis. I would also like to thank Prof. Tomisalv Lesičar, who was my mentor at the faculty for the purposes of this master thesis.

I would like to my grandfather Mario and my mother Kristina, for always supporting me in my decision to study mechanical engineering.

Finally, I would like to thank to all my friends and colleagues from the Stjepan Radić Student Dormitory for all the memories, adventures, and unforgettable moments.

Zagreb, January 2024 Davide Primc

SVEUČILIŠTE U ZAGREBU
FAKULTET STROJARSTVA I BRODOGRADNJE
Središnje povjerenstvo za završne i diplomske ispite
Povjerenstvo za diplomske ispite studija strojarstva za smjerove:
Procesno-energetski, konstrukcijski, inženjersko modeliranje i računalne simulacije i brodostrojarski

Sveučilište u Zagrebu Fakultet strojarstva i brodogradnje	
Datum	Prilog
Klasa: **602 - 04 / 24 - 06 / 1**	
Ur.broj: **15 - 24 -**	

DIPLOMSKI ZADATAK

Student: **Davide Primc** JMBAG: 0035210323

Naslov rada na hrvatskom jeziku: **Validacija modela plastičnosti i oštećenja aluminija 6014-T6**

Naslov rada na engleskom jeziku: **Validation of Plasticity and Damage Model for Aluminium 6014-T6**

Opis zadatka:

For modelling of deformation processes of systems or single components, numerical simulations nowadays represent an inevitable part of design process. However, numerical methods must be supplemented by proper constitutive relations of the material constitutive behaviour. Herein, choice of the constitutive law and calibration of the constitutive parameters by experimental investigation represents the most significant task. Accordingly, the task and purpose of this Master Thesis is the calibration of the material model for Aluminium 6014-T6. The calibration task consists of defining parameters of anisotropic elastoplasticity and softening during the quasi-static loading. Validation of the numerical results should be performed by comparison to the experimental measurements obtained for several types of specimens, covering tensional and shear stress states. For the experimental testing, test specimens are cut only in several orientations.
Based on everything said above in this study it is necessary to:

1. Study available literature on numerical modelling of the anisotropic elastoplasticity and ductile damage.
2. Calibrate hardening curve parameters of the material.
3. Calibrate ductile damage model parameters.
4. Validate the parameters obtained by comparing results of the finite element simulations against experimental measurements.

During thesis preparation one must comply with the standard rules for preparation of master thesis. It is necessary to list all literature used and received assistance.

Zadatak zadan:	Datum predaje rada:	Predviđeni datumi obrane:
16. studenoga 2023.	18. siječnja 2024.	22. – 26. siječnja 2024.

Zadatak zadao:

Doc. dr. sc. Tomislav Lesičar

Predsjednik Povjerenstva:

Prof. dr. sc. Tanja Jurčević Lulić

Contents

List of Figures

List of Tables

List of Symbols

$\mathbf{A}$	Strength coefficient, $\mathrm{N/mm^2}$
$\mathrm{c_d}$	Dilatational wave speed, mm/s
E	Young's modulus, MPa
I	Vector of internal forces, N
$\mathrm{k_0}$	Initial yield stress, MPa
$\mathrm{L_{min}}$	Smallest element length, mm
M	Nodal mass matrix, kg
$\mathbf{n}$	Strain hardening exponent, $-$
P	Vector of external forces, N
Q	Stress difference between saturated and yield stress, MPa
t	Time, s
$\mathrm{\ddot{u}}$	Vector of nodal acceleration, $\mathrm{mm/s^2}$
$\mathrm{\dot{u}}$	Vector of nodal velocities, mm/s
u	Displacement vector, mm
α	Weighting factor, $-$
β	Strain coefficient, $-$
ρ	Density, $\mathrm{kg/mm^3}$
$\bar{\varepsilon}_\mathrm{p}$	True effective plastic strain, $-$
ε_o	Initial yield point, $-$
$\varepsilon_\mathrm{ij}^\mathrm{p}$	Plain strain tensor, $-$
σ_Y	Yield strength, MPa
σ_ij	Stress tensor, MPa

Sažetak

Automobilska industrija jedna je od najvećih svjetskih industrija te je predvodnik u raznim inovativnim inženjerskim rješenjima. Uslijed sve većih ekoloških reformi klasična automobilska industrija pomalo, ali sigurno izumire. Upotreba konvencionalnih motora s unutarnjim izgaranjem sve se više zamjenjuje električnim pogonom. Električni automobili dobivaju električnu energiju iz baterijskog sustava koji je najčešće smješten u podvozju vozila. U slučaju sudara može doći do kratkog spoja baterija, kratki spoj baterija dovodi do požara koji je izuzetno teško ugasiti. Kako bi se zaštitili korisnici, baterijski sustavi se postavljaju u aluminijska kućišta koja ih štite u slučaju udara. Aluminijske legure imaju nisku gustoću, visoku čvrstoću i dobru duktilnost. Duktilnost aluminijskih legura je ta koja osigurava apsorpciju energije prilikom udara. Radi optimalnog konstruiranja kućišta baterija, potrebno je poznavati točna svojstva korištene legure te njezino konstitutivno ponašanje prilikom razvoja duktilnog oštenjenja uslijed opterećivanja.

U ovome radu analizirana je 6014-T6 aluminijska legura koja se često koristi u automobilskoj industriji. Na početku je prikazana teorijska pozadina elastoplastičnog i anizotropnog ponašanja materijala i ponašanje materijala uslijed duktilnog oštećenja. Kako bi se konstitutivno ponašanje materijala čim točnije opisalo u numeričkim simulacijama, provedena su eksperimentalna ispitivanja na različitim vrstama uzoraka kako bi se opisalo što više stanja naprezanja u materijalu. Za opis elastoplastičnog ponašanja materijala korišten je kombinirani Swift-Voce zakon tečenja, čiji su parametri određeni eksperimentalno-numeričkom procedurom. Za opis anizotropnog ponašanja korišteni su Hill 48 i Barlat Yld2000 zakoni tečenja, čiji su parametri također određeni eksperimentalno-numeričkom procedurom. U radu je korišten Hosford-Coulomb model popuštanja za opisivanje duktilnog oštećenja, te opisana je procedura za određivanje parametra ovog zakona. Numeričke analize provedene su u programskom paketu *Abaqus*, rezultati simulacija validirani su rezultatima eksperimentalnih mjerenja.

Ključne riječi: elastoplastično ponašanje, Swift-Voce zakon tečenja, anizotropno ponašanje, duktilno oštećenje, metoda konačnih elemenata

Contents

The automotive industry is one of the largest industries in the world and a leader in many innovative engineering solutions. Due to increasing environmental reforms, the traditional automotive industry is slowly but surely dying out. Conventional internal combustion engines are being increasingly replaced by electric motors. Electric cars receive their electrical energy from a battery pack, which is usually located in the vehicle's chassis. In the event of a collision, a short circuit can occur in the battery pack, which can lead to a fire that is extremely difficult to extinguish. To protect its users, battery packs are located in aluminum housings that protect them in the event of a collision. Aluminium alloys have low density, high strength, and good ductility. For optimal battery housing design, it is necessary to know the exact properties of the alloy used and its behavior during the development of ductile fracture due to loading.

In this paper, the 6014-T6 aluminium alloy, which is commonly used in the automotive industry, was analyzed. The theoretical background of elastoplastic and anisotropic material behavior and including the behavior of the material due to ductile damage are presented at the beginning. In order to describe the constitutive behavior of the material as accurately as possible in numerical simulations, experimental tests were performed on various types of samples to describe as many stress states as possible in the material. The combined Swift-Voce flow law was used to describe the elastoplastic behavior of the material, and its parameters were determined by an experimental-numerical procedure. The Hill 48 and Barlat Yld2000 yield laws were used to describe the anisotropic behavior, and their parameters were also determined by an experimental-numerical procedure. The Hosford-Coulomb model was used to describe ductile damage, and the paper outlines the procedure for determining its parameters. The numerical analyses were performed using the *Abaqus* software package, and the simulation results were validated against the results of experimental measurements.

Keywords: elastoplastic behavior, Swift-Voce hardening law, anisotropic behaviour, ductile damage, finite element method

Prošireni sažetak

Ovaj rad izrađen je u suradnji s hrvatskom tvrtkom AVL-AST d.o.o. te austrijskom tvrtkom AVL List GmbH. Navedene tvrtke bave za razvojem, testiranjem i proizvodnjom pogonskih sustava i naprednih tehnologija vozila.

Električni pogon vozila sastoji se od baterijskih sklopova u kojima je pohranjena električna energija, pretvarača koji pretvara istosmjernu struju iz baterijskog sklopa u izmjeničnu struju, te elektromotora koji daju pogon, te upravljačke jedinice koja sve kontrolira. Baterijski sklopovi smješteni su kućištima i najčešće se nalaze u podvozju vozila. U slučaju sudara može doći do kratkog spoja baterija, kratki spoj baterija dovodi do požara koji je izuzetno teško ugasiti. Iz tog razloga kućišta moraju biti konturirana kako bi spriječile bilo kakvo oštećenje baterijskog sklopa. Najkorišteniji materijal za izradu baterijskih kućišta su upravo aluminijske legure. Aluminijske legure imaju nisku gustoću, pa aluminijske komponente pridonose znatnom povećanju mase vozila. Osim toga, relativno visoka čvrstoća i duktilnost omogućuju dovoljnu deformabilnost i apsorpciju energije prilikom prometnih nezgoda. Konstruiranje baterijskog paketa je skup i dugotrajan proces, potrebno je provesti mnogobrojna istraživanja i testova kako bi se osigurao mehanički integritet, a i samim time sigurnost tijekom korištenja. Fizički testovi su izuzetno skupi, te zahtijevaju puno vremena, što sve dovodi do produljenja procesa konstruiranja i izrade, te do skupljeg konačnog proizvoda. Iz tog razloga, u zadnje vrijeme sve se više pribjegava korištenju numeričkih simulacija u procesu konstruiranja baterijskih sklopova. Tako se pojednostavljuje i skraćuje proces izrade konačne komponente. Za točnu statičku ili dinamičku numeričku analizu sudara baterijskog sklopa, potrebno je poznavati točna svojstva korištenih materijala, te implementirati materijal u softver za numeričke simulacije. Kako bi se odredila svojstava materijala tijekom procesa deformiranja i razvoja duktilnog oštećenja, potrebno je provesti eksperimentalna mjerenja na uzorcima. Na osnovu eksperimentalnih rezultata, provodi se kalibracija numeričkog modela anizotropnog elastoplastičnog ponašanja materijala kao i kalibracija inicijacije i razvoja duktilnog oštećenja.

U prvom poglavlju dan je kratki opis upotrebe aluminijskih legura u automobilskoj industriji, te prednosti korištenja istih.

U drugom poglavlju opisana su svojstva aluminijske legure 6014-T6, te korišteni materijalni modeli. Opisana je teorijska pozadina izotropnog i anizotropnog ponašanja materijala. Također, opisuje se kombinirani zakon tečenja Swift-Voce i dva različita anizotropna zakona tečenja, Hill 48 i Barlat Yld2000. Poglavlje pokriva osnovne principe i teoriju duktilnog oštećenja, kao i njezinu implementaciju u programu *Abaqus*. Objašnjen je Hosforth-Coulomb model oštećenja koji je korišten u radu.
U trećem poglavlju predstavljen je eksperimentalni postupak korišten za kalibraciju. Sva ispitivanja provedena su na Sveučilištu ETH u Zurichu.
U četvrtom poglavlju opisan je korišteni simulacijski model te postupak za određivanje parametara Swift-Voce zakona, raspravljaju se rezultati dobiveni korištenjem spomenutoga zakona tečenje.
U petom poglavlju opisan je postupak za određivanje parametara Hill 48 i Yld2000 zakona te se raspravljaju rezultati dobiveni korištenjem ova dva anizotropna zakona tečenja.
U šestom poglavlju opisan je postupak za određivanja parametara Hosford-Coulomb i raspravljaju se rezultati dobiveni korištenjem zakona o duktilnom oštećenju.
Napokon, zaključci ovog rada i preporuke za buduće radove izneseni su u završnom poglavlju ovog diplomskog rada.

1 Introduction

The automotive industry is going through a major change. In the last couple of decades, global warming has changed public and political opinion regards to car transportation. Huge efforts are put into lowering fuel consumption and CO2 emissions. In recent years, global car regulations have become increasingly stringent, pushing the entire industry to explore innovative solutions for car development. This has led to a renewed focus on research and development, with manufacturers investing heavily in new technologies and processes to meet harsh new regulations. Vehicles are getting bigger and heavier with every new generation [1], Figure 1.1 shows the second generation of the Porsche 991 from 1970 to the seventh generation from 2018.

Figure 1.1: Porsche [2]

This larger size naturally leads to increased weight, and to make the problem worse the number consumer electronics installed in cars is only increasing, only worsening the problem. To combat this increase in weight car manufactures have turned to an ever increasing use of aluminium alloys. In comparison with steel alloys, that has been the main material for the automotive industry for decades, aluminium has a better strength to weight ratio. Hence, despite the fact that steel possesses a greater tensile strength, it is nearly three times more dense compared to aluminium. For this reason, aluminium alloys offer a weight advantage. Besides that, aluminium is more malleable than steel, which means it can be easily formed in all kinds of shapes and for extruding complicated cross sections without it starting to break or crack. In addition, extruded aluminium profiles can absorb almost twice the crash energy than steel alloys [1]. A real world example would be more appropriate. The chassis of a modern electric car, seen in Figure 1.2, is composed of a combination of steel and aluminium alloys.

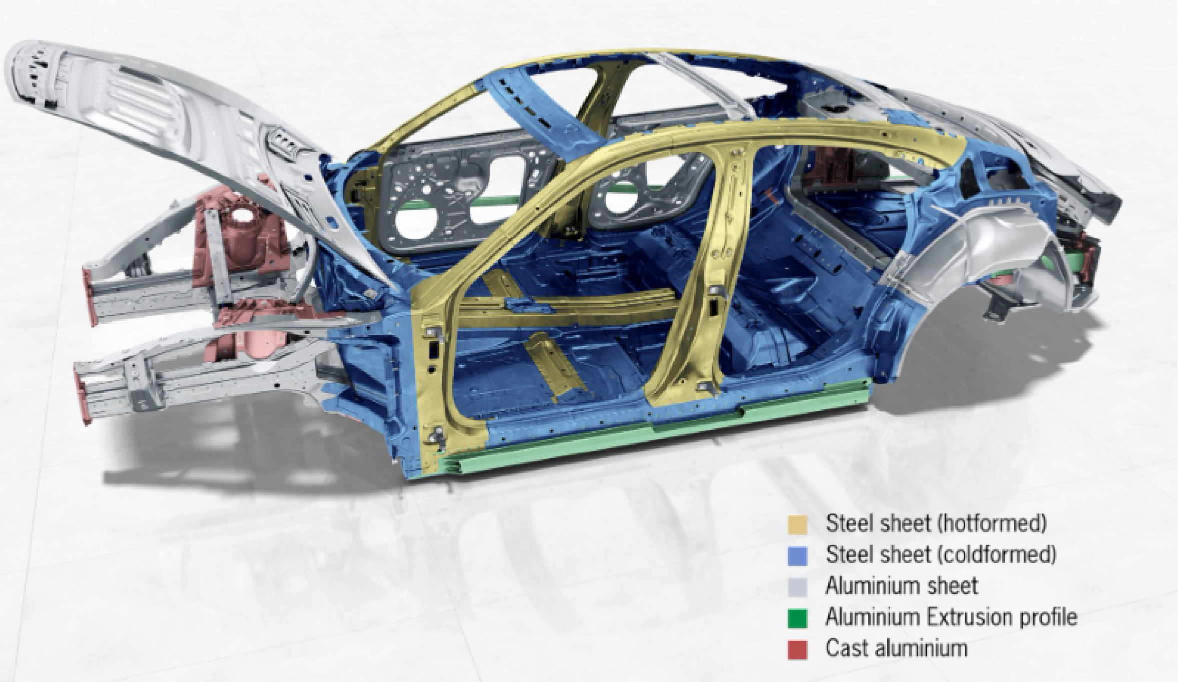

Figure 1.2: Porsche Taycan chassis [3]

The strut mounts, axle mounts and the rear side members are made of die-cast aluminium. The shock absorber mounts are forged aluminium. The front side members combine an aluminium shell construction with extruded sections, ideal for absorbing

energy during a collision. To that, almost the complete outer skin is made from aluminium. On the other hand the passenger cell, also called the safety cage, is made almost exclusively of steel alloys. High-strength hot-formed steels provide enhanced protection to passengers in the event of a collision. In this particular application, the weight penalty of using steel alloys was justified by the increased safety it provided to the passengers [3].
A new challenge facing the automotive industry is the design of the battery pack. The battery pack, as well the entire drivetrain can be seen in the Figure 1.3.

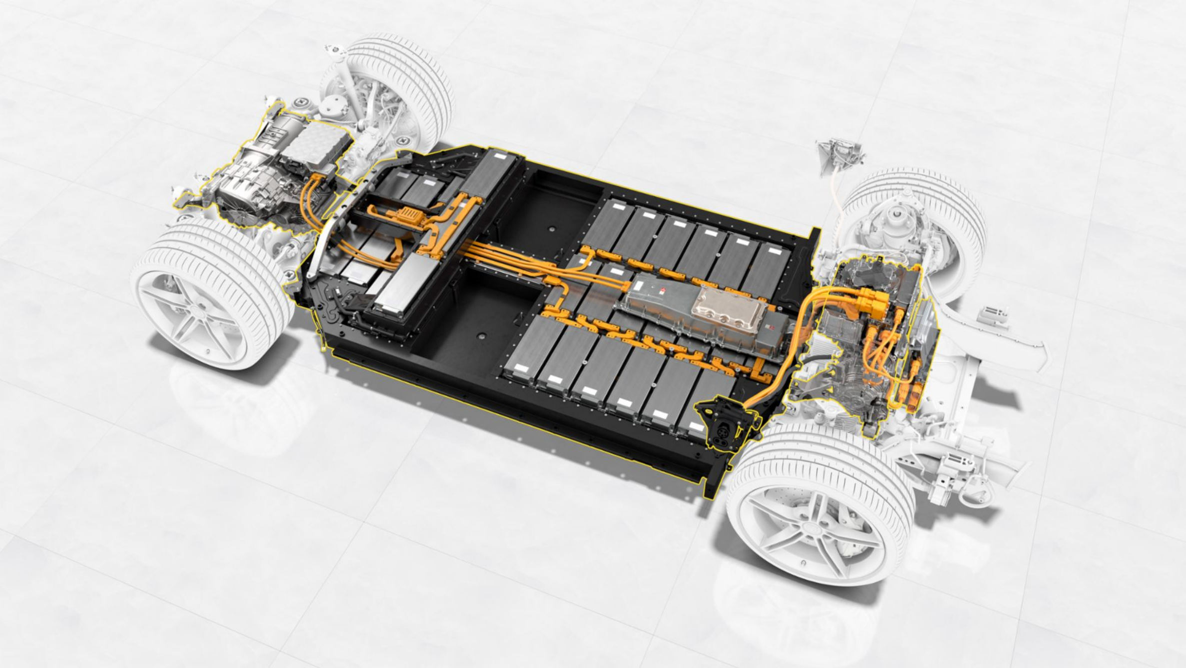

Figure 1.3: Porsche Taycan battery pack [4]

Battery pack need to be watertight and are usually a sandwich construction, consisting of a cover at the top and a bulkhead plate at the bottom. The truss-design battery frame with multiple subdivisions is located in between the cover and the bulkhead plate. The individual cells are stacked together to form a unit called a cell module. These cell modules are then connected in series or parallel configurations using wires or bussbars, which allows them to work together to provide the desired voltage and current output for the battery pack. Individual cells present a significant fire hazard. Therefore, it is of the most importance to prevent any kind of protrusion into the battery pack. Extruded aluminium is commonly used for battery pack housings and crash structure, both inside and outside the battery pack [4].

1.1. Thesis structure overview

The aim of this thesis is to correctly predict the hardening, anisotropy, and damage response of 6014-T6 aluminium under quasi-static loading. In the first chapter, a brief description of usage aluminium alloy usage in the automotive industry is given.
Chapter 2 discusses 6014-T6 aluminium properties and the material models that have been used to describe it. The theoretical background of both isotropic and anisotropic yielding is described. The combined Swift-Voce flow law is explained and two different anisotropic yield law are described, Hill 48 and Barlat Yld2000. It also covers basic principles and theory of the ductile damage, as well as its implementation into *Abaqus*. The Hosforth-Coulomb damage model used in the thesis, is explained in more detail.
Chapter 3 presents the experimental setup used for the calibration, all the experiments were preformed by the ETH Zurich university.
Chapter 4 presents the procedure for the determination of the combined Swift-Voce hardening law parameters and the results obtained using the plastic hardening law are discussed.
Chapter 5 presents the procedure for the determination of the Hill 48 and Yld2000 parameters and the results obtained using the two anisotropic hardening law are discussed.
Chapter 6 presents the procedure for the determination of the Hosford-Coulomb parameters and the results obtained using the ductile damage law are discussed.
Finally, the conclusions of this work and recommendations for future works are presented in the final chapter of this thesis.

2 Material model

2.1. 6014-T6 aluminium alloy

Aluminium and its alloys are the most versatile, economical, and attractive metallic materials in the world, due to the unique combination of mechanical properties. Aluminium alloys are second to steels in use as structural metals. With a low density of only 2700 kg/m^3 and with high strength and ductility, aluminium is ideal for the design and construction of strong, yet lightweight structures. In addition, aluminium is extremely resistant to atmospheric corrosion, due to its tendency to form a compact oxide layer over the surface. It can also resist corrosion by water, salt, and other environments if it is appropriately alloyed and treated. Aluminium can be fabricated in any desired form. It can be cast in any form, rolled, forged, hammered, stamped, drawn, spun formed or milled. Furthermore, the metal can be extruded into a wide range of profiles, with almost no limitations.

Aluminium alloys are usually divided into two categories: wrought and cast compositions. A nomenclature for different types of wrought and cast alloys has been developed by the Aluminum Association and its designation system is widely accepted in the world [5]. Their alloy identification system employs different nomenclatures for wrought and cast alloys, but divides alloys into families for simplifications. For wrought alloys a four-digit system is used to produce a list of wrought composition families. For instance, the primary alloying element is labeled by the first number of alloy designation and this element produces a group of alloys with similar properties. The second number denotes whether it is a modification of an existing alloy and the last two digits are assigned sequentially by the association. Examples of aluminium wrought alloy families are listed in Table 2.1.

Table 2.1: Wrought Alloy Designation System and Characteristics [5]

Series Number	Primary Alloying Element	Relative Corrosion Resistance	Relative Strength	Heat Treatment
1xxx	None	Excellent	Fair	Non-heat-treatable
2xxx	Copper	Fair	Excellent	Heat-treatable
3xxx	Manganese	Good	Fair	Non-heat-treatable
4xxx	Silicon	Fair	Fair	Non-heat-treatable
5xxx	Magnesium	Good	Good	Non-heat-treatable
6xxx	Magnesium and silicon	Good	Good	Heat-treatable
7xxx	Zinc	Fair	Excellent	Heat-treatable

In addition to the huge variety of alloys that are available, the temper of each alloy can create considerable differences in their characteristics. As it can be seen in Table 2.1, there are heat treatable and non-heat treatable aluminium wrought alloys. Alloys in the non-heat-treatable group can not be strengthened significantly by heat treatment, and their properties depend upon the degree of cold work. On the other hand, heat treatable alloys have increased strength beyond the strengthening effect of adding alloying elements. Both heat treatable and non-heat treatable alloys can be strengthen by strain-hardening (cold working), which is achieved by mechanical deformation of the material at ambient temperature. As the material is strain-hardened, it becomes resistant to further deformation and its strength increases. This strain-hardened alloy can be heat treated to stabilize properties so that strength does not decrease over time (age softening). Firstly, the material can be solution heat treated. This allows soluble alloying elements to enter into solid solution; they are retained in a supersaturated state upon quenching, a controlled rapid cooling usually performed using air or water. Next, the material may undergo a precipitation heat treatment, also called artificial aging, by which constituents are precipitated from a solid solution to increase the strength.

The primary alloying elements of 6xxx series are magnesium and silicon in proportions that form magnesium silicide ($Mg2Si$). Despite the lower strength than 2xxx and 7xxx series alloys, 6xxx series alloys are widely used in architecture, marine and automotive industry, due to their excellent formability, weldability, machinability, and corrosion resistance. However, the most important advantage of these alloy series is extreme extrudability in combination with good strength [6]. The 6014-T6 alloy is one of the most popular alloys in the automotive industry. It is used for the construction of the vehicle body structures profile structures and the battery housings. Mechanical properties of the 6014-T6 aluminium alloy are displayed in Table 2.2.

Table 2.2: Mechanical properties of the 6014-T6 aluminum alloy [5]

Density $[\mathrm{kg/m^3}]$	Young's Modulus [MPa]	Poisson ratioo [−]	Yield stress [MPa]	Ultimate tensile stress [MPa]
2700	75150	0.33	190	220

2.2. Isotropic yield

In order to correctly predict the behaviour and damage of components and structures, it is necessary to develop a material model which corresponds to the real material. Material properties such as Young's modulus, Poisson ratio, ultimate tensile strength, yield strength, and stress-strain relationship are identified through the uniaxial tensile test. Material hardening is usually described by the hardening laws which are analytical expressions used to fit the plastic region of an experimental true stress-strain data. According to [7] the combined Swift-Voce hardening law is the most suitable for the numerical modelling of aluminium alloys. It is a linear combination of Swift and Voce isotropic hardening laws. During isotropic hardening, the yield surface expands equally in all directions of the stress space while its shape remains constant. In this thesis, the isotropic yielding was described by the Von Mises yield criterion:

$$f(\sigma_{ij}, \varepsilon_{ij}^p) = \frac{1}{\sqrt{2}}\sqrt{(\sigma_1-\sigma_2)^2+(\sigma_2-\sigma_3)^2+(\sigma_3-\sigma_1)^2} - \sigma_Y(\varepsilon_{ij}^p), \tag{2.1}$$

where σ_Y is the yield stress in uniaxial tension and σ_i are the principal stresses. The Von Mises yield criterion is illustrated in Figure 2.1, in planar loading conditions ($\sigma_3 = 0$) it is represented by an ellipse.

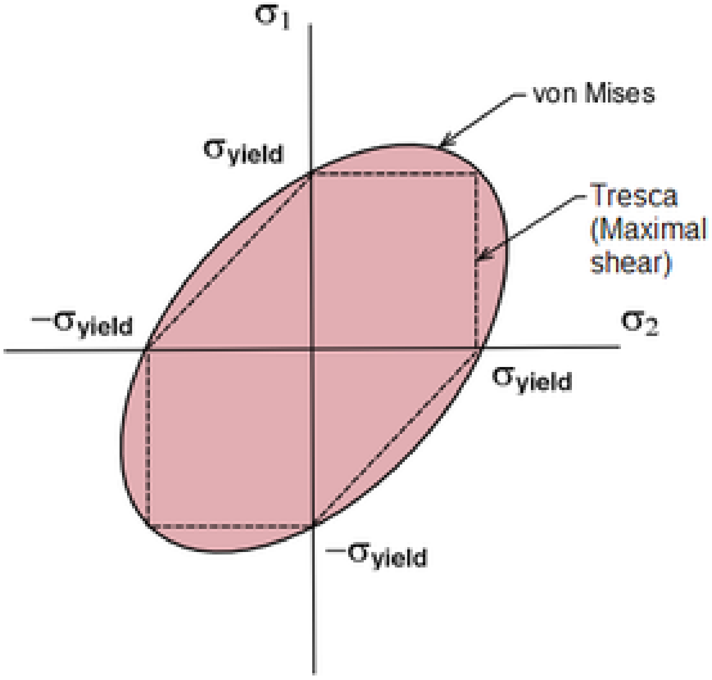

Figure 2.1: Von Misses yield surface [8]

The yield stress σ_Y is related to the effective plastic strain, and it functional dependence on the effective plastic strain is given by the universal flow hardening curve of the material. The combined Swift-Voce hardening law is used to describe this functional dependence. Swift law is a power law and it is defined as:

$$\sigma_s(\bar{\varepsilon}_p) = A(\bar{\varepsilon}_p + \varepsilon_0)^n, \tag{2.2}$$

in which the material coefficients are elastic strain at the initial yield point (ε_0), strength coefficient (A), and strain hardening exponent (n), while $\bar{\varepsilon}_p$ is the true effective plastic strain. Voce hardening law is exponential law and it is described by the following equation:

$$\sigma_v(\bar{\varepsilon}_p) = k_0 + Q(1 - e^{-\beta\bar{\varepsilon}_p}), \tag{2.3}$$

in which the material coefficients are initial yield stress (k_0), stress difference between saturated and initial stress (Q), and the strain coefficient (β). The final hardening curve of the combined Swift-Voce hardening law is approximated by linear combination of the power and exponential law:

$$\sigma_Y = \alpha \cdot \sigma_s + (1 - \alpha) \cdot \sigma_v, \tag{2.4}$$

where α is the weighting factor. It can be seen in Figure 2.2, the Voce law exhibits a saturation hardening behaviour, while the Swift law exhibits non-saturation hardening behaviour at high plastic strains. The linear combination of Swift and Voce law incorporates both saturating and non-saturating material behaviour through the use of the weighting factor α.

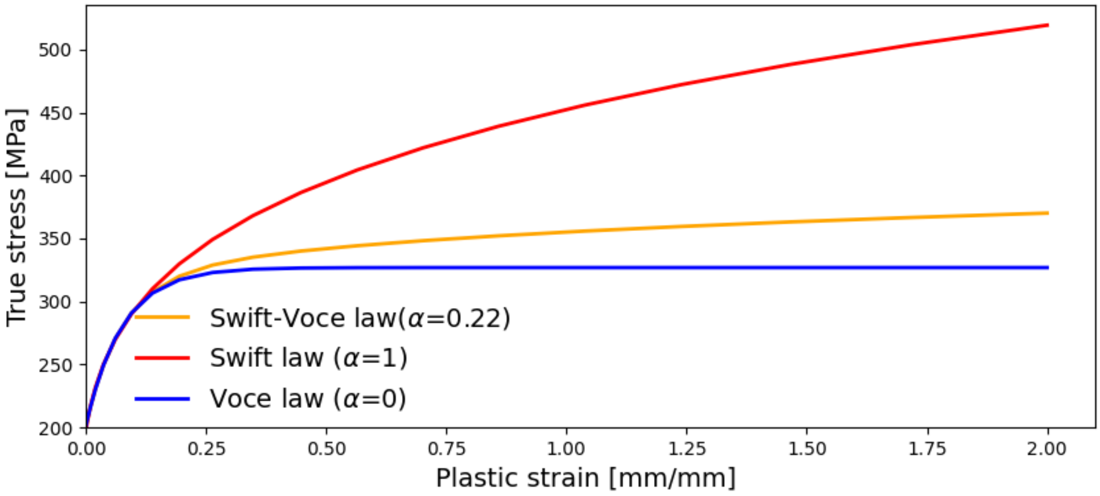

Figure 2.2: Stress-strain curves for Swift, Voce and Swift-Voce laws

The 6014-T6 alloy material coefficients were obtained through curve fitting of experimental true stress-plastic strain data up to the point of necking onset. The Figure 2.3 illustrates the implemented workflow used for the calibration of the Swift-Voce hardening law. The input for the calibration is the force-displacement curves obtained from the UT (uniaxial tension) specimens. The data has been first transformed to engineering stress-engineering strain data, and subsequently to true stress-true strain data. It is important to emphasize that this transformation is valid only until the UTS (ultimate tensile strength) point, which is also onset of the significant necking.

The true strain has been converted to plastic strain, which is suitable for determining the Swift and the Voce material coefficients. The true stress-plastic strain points were approximated using the Swift law equation and the Voce law equation thought curve fitting. The two laws were calibrated individually, and subsequently, another curve fitting analysis was conducted to calibrate the α weighting factor.

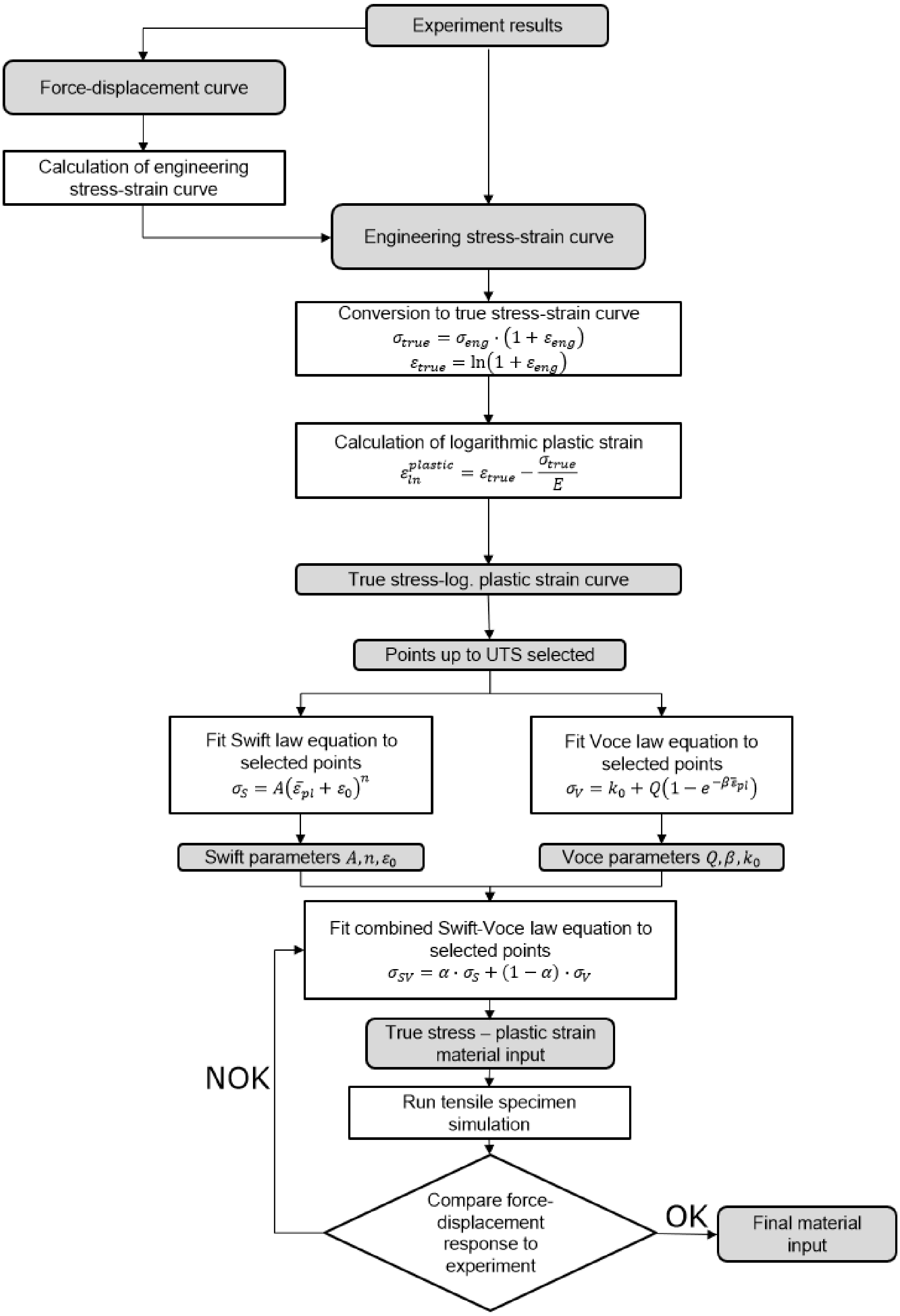

Figure 2.3: Swift-Voce material coefficients determination workflow

2.3. Anisotropic yield

Sheet forming is a crucial manufacturing process, sheet metals often show anisotropic properties due to previous thermo-mechanical actions such as annealing and rolling. In this case, the material displays orthotropic behavior, meaning the mechanical properties are symmetric in three perpendicular planes. To enhance the accuracy of the numerical simulation, a precise description of the anisotropic properties is needed. To achieve this, anisotropic yield functions were used, different yield surfaces are shown in Figure 2.4.

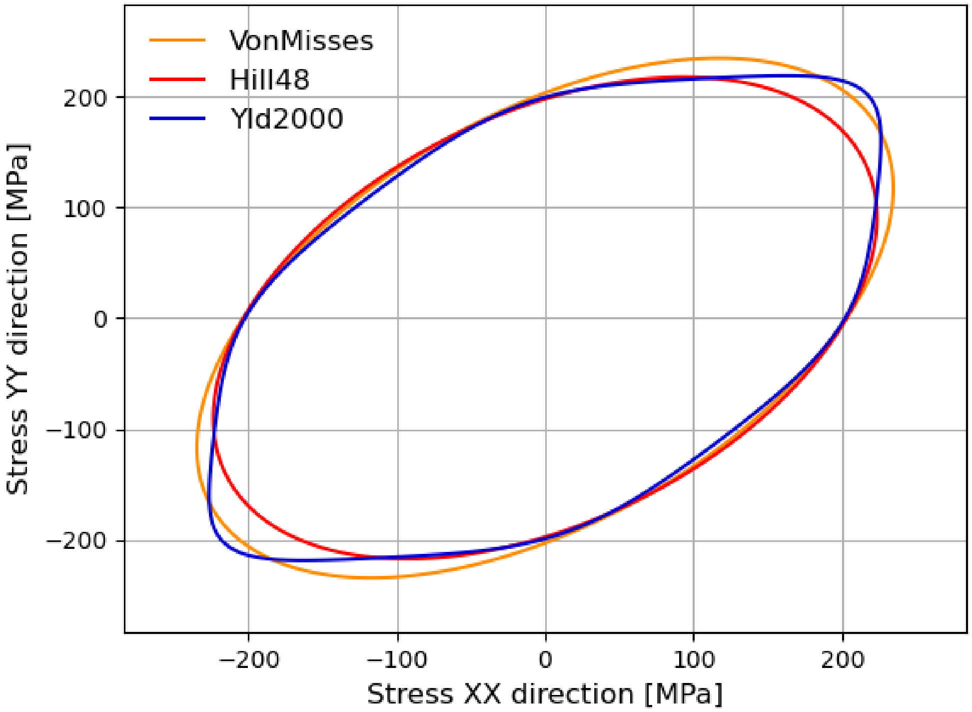

Figure 2.4: Yield surfaces

The von Mises yield surface (orange curve) is showing the isotropy of the material while the Hill 48 yield surface (red curve) and Yld2000 yield surface (blue curve) are showing the anisotropy of the material. It is evident from the Figure 2.4 that the von Mises yield surface exhibits constant material strength regardless of the stress state, whereas the other two surfaces display variations in material strength based on the stress state. Anisotropic yield properties come in various forms from manufacturing processes and exhibit different yield values in the rolling and transverse direction as shown in Figure

2.5. To determine the anisotropic behaviour of metal sheets, the stress ratio and the Lankford ratio are calculated.

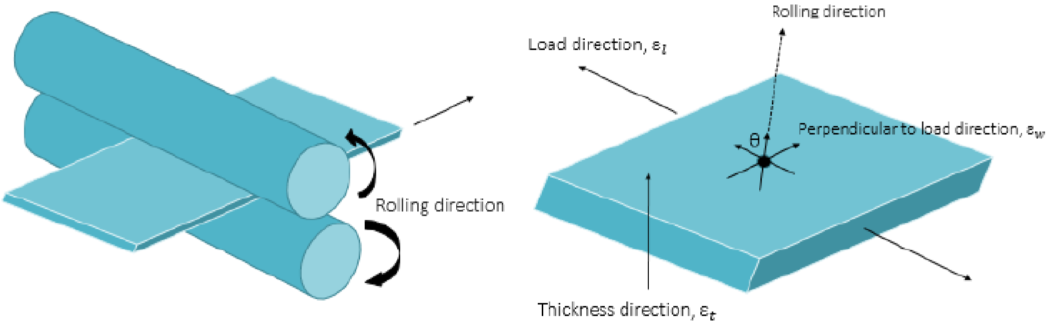

Figure 2.5: Rolling direction during a manufacturing process [9]

The Lankford ratio r_θ is defined as the ratio of width-to-thickness plastic strain increments, its calculated by the equation [9]:

$$r_\theta = \frac{\varepsilon_w}{\varepsilon_t}, \tag{2.5}$$

where ε_w is the width strain, and ε_t is the thickness strain. The thickness strain is difficult to measure accurately in a thin sheet, so it is calculated from the longitudinal and width strains by assuming the volume remains constant. Thus, the equation is redefined:

$$r_\theta = \frac{\varepsilon_w}{-(\varepsilon_l + \varepsilon_w)}, \tag{2.6}$$

where ε_l is the longitudinal strain. The in-plane strain ε_t and ε_w are obtained from the experiments. A more physical way to understand the Lankford ratio is to think of it as the ratio of thinning to necking of the test specimen.

On the other hand, the stress ratio R_θ is the ratio of stress in the extrusion direction to the stress in another direction:

$$R_\theta = \frac{\sigma_{Y,\theta}}{\sigma_{Y,0}}, \tag{2.7}$$

where $\sigma_{Y,0}$ is the yield stress in the extrusion direction, and $\sigma_{Y,\theta}$ is the yield stress at angle relative to the extrusion direction. A stress ratio greater than one indicates that the material has strengthened, while a value less than one indicates that the material has weakened. In the thesis, two anisotropic models were utilized: the Hill 48 model, which is available in the *Abaqus* software, and the Barlat Yld2000 model, which is not implemented in *Abaqus*. The latter was run using a user subroutine, the subroutine was provided thy the ETH Zurich University.

The quadratic Hill 48 yield criterion is deviatoric stresses dependent, but is pressure independent. It predicts the same yield stress in tension and in compression. The Hill 48 yield criterion is defined by the equation [9]:

$$2f(\sigma_{ij}) = F(\sigma_{22} - \sigma_{33})^2 + G(\sigma_{33} - \sigma_{11})^2 + H(\sigma_{11} - \sigma_{22})^2 + 2N\sigma_{12}^2 = 1, \tag{2.8}$$

where F, G, H, N are the independent anisotropic coefficients determined experimentally and σ_{ij} are the normal and shear stress components.

Barlat yield criterion is highly used in plasticity, damage, and metal formation [9], several Barlat criterion exists:

- Barlat's 89: A yield function for orthotropic sheets under plane stress conditions,
- Barlat's 91: A six-component yield function for anisotropic materials,
- Yld2000-2D: Plane stress yield function for aluminium alloy sheets,
- Yld2004-18p: Linear transformation-based anisotropic yield functions.

The non-quadratic Barlat Yld2000-2D yield criterion is denoted by the equation [10]:

$$f(\sigma_{ij}) = 2^{-\frac{1}{\alpha_0}} \left(|S'_I - S'_{II}|^{\alpha_0} + |S'_I + 2S'_{II}|^{\alpha_0} + |2S''_I + S'_{II}|^{\alpha_0}\right)^{\frac{1}{\alpha_0}} = 1 \tag{2.9}$$

where S'_I, S'_{II} are the principal stress values , S''_I, S''_{II} are the linearly-transformed Cauchy stress vectors, and α_0 is 6 for FFC (face-centered cubic) metals.
The material coefficients were obtained through curve fitting of experimental stress ratios and Lankford ratios. The implemented workflow used for the calibration is illustrated in the Figure 2.3. The two ratios were obtained by dividing the true stress-plastic strain data taken at the 15°, 30°, 45°, 60°, 75°, and 90° orientation and by the corresponding data at the 0° orientation. It is important to point up that ratios aren't a constant, the ratios change during the loading step, for this reason they were extracted at their saturated values. The experimental stress ratios and Lankford ratios were approximated using the Hill 48 law equation and the Yld2000 law equation.

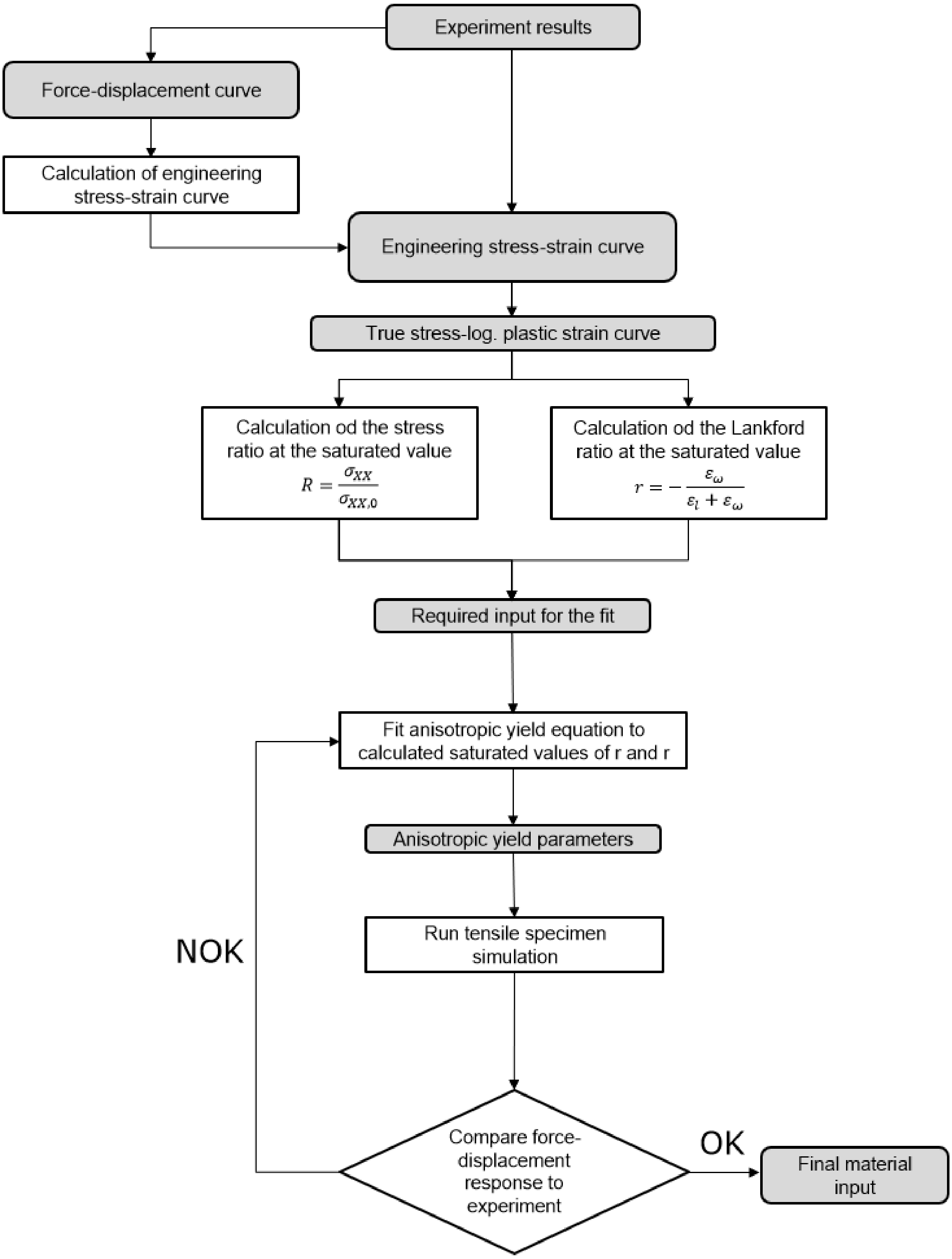

Figure 2.6: Hill 48 and Yld2000 material coefficients determination workflow

2.4. Progressive damage and failure

Two different types of fracture exist, brittle and ductile fracture. Brittle fracture is characterised by having little or no plastic deformation prior to failure. Crack growth in brittle materials is sudden, as the whole fracture energy is concentrated in the crack tip. On the other hand, ductile fracture is characterised by large plastic deformation and necking. Due to the dulling of the crack tip the material resist the crack growth and absorbs energy in the process. Some of the benefits of using ductile materials as engineering materials include:

- high deformability: ductile materials exhibit significant plastic deformation before fracture, allowing them to absorb energy in the process,
- resistance to brittle fracture: ductile materials are less prone to sudden brittle fracture, critical in applications where impact or sudden load is involved,
- enhanced structural integrity: ductile materials can distribute stress more effectively and can accommodate non-uniform loads,
- ease of fabrication: ductile materials are often easier to shape, form, and weld.

Ductile fracture is a well known physical process that leads to the formation of cracks in metals due to the nucleation, growth and coalescence of voids. Ductile fracture is a result of the material's structural imperfections that lead to the formation of voids, shown in Figure 2.7 at stage 1. As the material undergoes plastic deformation, existing voids expand and new ones form, reducing the material's internal resistance, seen in Figure 2.7 at stage 2. The porosity of the material increases due to void growth and nucleation, resulting in the formation of a primary localization band at the mesoscale, seen in Figure 2.7 at stage 3. The inter-void spacing determines the width of this primary band [11]. As a result, void growth and nucleation in the primary localization band are accelerated, as seen in stage 4 of Figure 2.7. This leads to a sharp increase in porosity and the number of voids within the primary localization zone. As the material is subjected to further loading, the mechanical fields around individual primary voids begin to interact, causing the nucleation and growth of voids within secondary bands of localization at the microscale (Figure 2.7 at stages 5 and 6). These bands are often several orders of magnitude smaller than the primary localization band. The coalescence of voids within the secondary localization band creates and expands macroscopic cracks (Figure 2.7 at stage 7), ultimately resulting in material failure [11].

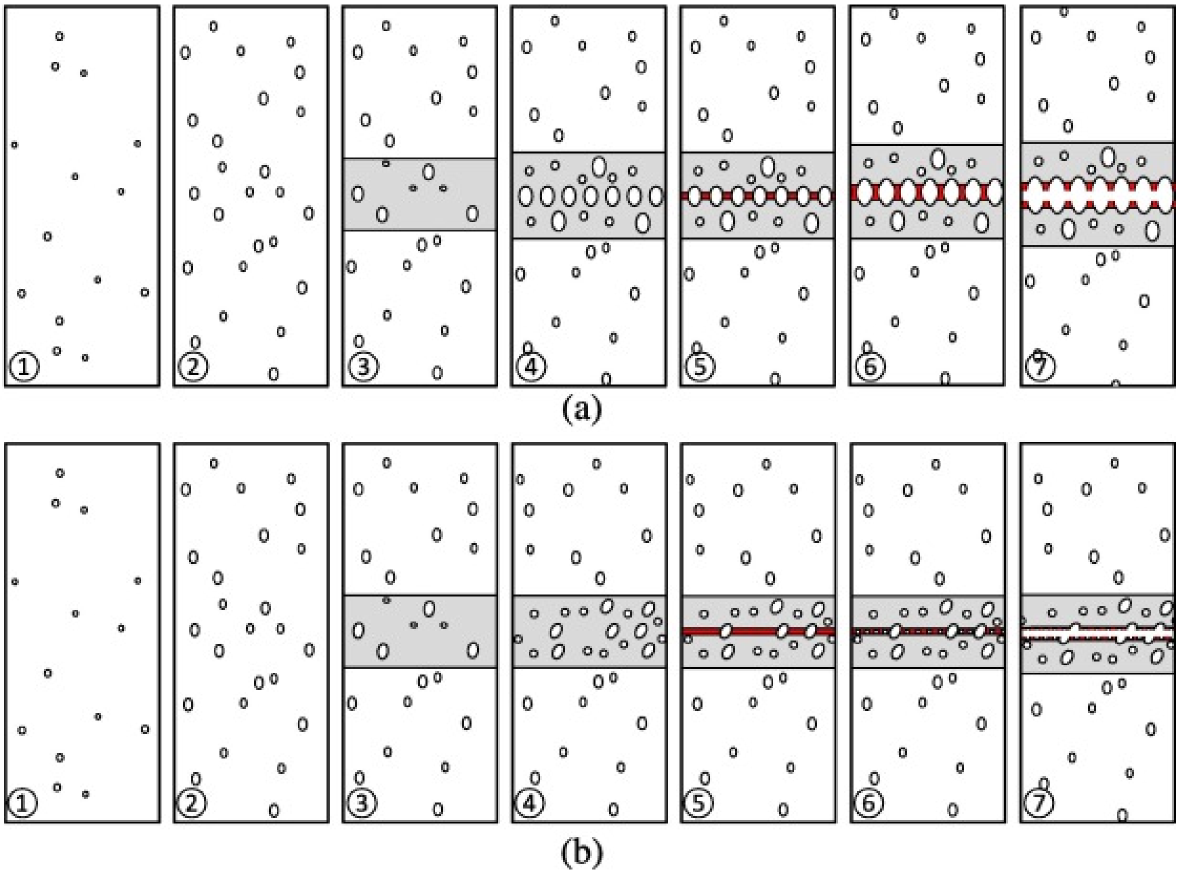

Figure 2.7: Ductile fracture process with coalescence through (a) internal necking, and (b) void sheet fracture [12]

In addition, numerous ductile damage models have been developed to predict the amount of damage due to the nucleation, growth, and coalescence of microcracks within the material. In an attempt to model ductile damage, different authors have proposed several approaches, each of them leading to a number of damage models [13]. The problem lies in that most of them aren't suitable to be used in the industry. There are many reasons, but to name a few, the damage models aren't implemented in commercially available finite element software packages, the calibration takes too much time and effort, and more often than not, they are too complicated to be used. The reality is that a simulation engineer has too many tasks to tackle to worry himself with damage models that take months to calibrate.

2.4.1. Hosford-Coulomb criterion

Based on micromechanical considerations the Hosford-Coulomb (HC) criterion is used to predict ductile fracture initiation in polycrystalline materials [10]. The model defines the equivalent plastic strain at the instant of fracture as a function of the stress state. The stress state is described by the stress triaxiality η and the Lode angle parameter $\bar{\theta}$. The stress triaxialiy is described with the equation [10]:

$$\eta = -\frac{\sigma_m}{\sigma_{eff}}, \tag{2.10}$$

where σ_{m} is the mean stress, σ_{eff} is the Mises equivalent stress. The Lode angle parameter is described with the equation [10]:

$$\bar{\theta} = 1 - \frac{2}{\pi} cos^{-1} \left(\frac{27}{2} \frac{J_3}{\sigma_{eff}^3} \right), \tag{2.11}$$

where J_3 is the third invariant of the Cauchy stress deviator. While the physical meaning of the stress triaxiality can be easily comprehended, the Lode angle parameter lacks an intuitive physical interpretation. One way to understand it is that, for a given stress triaxiality, there exist an infinite number of stress states that can be characterized by an additional parameter, the Lode angle parameter. The possible stress states can be seen in Figure 2.8.

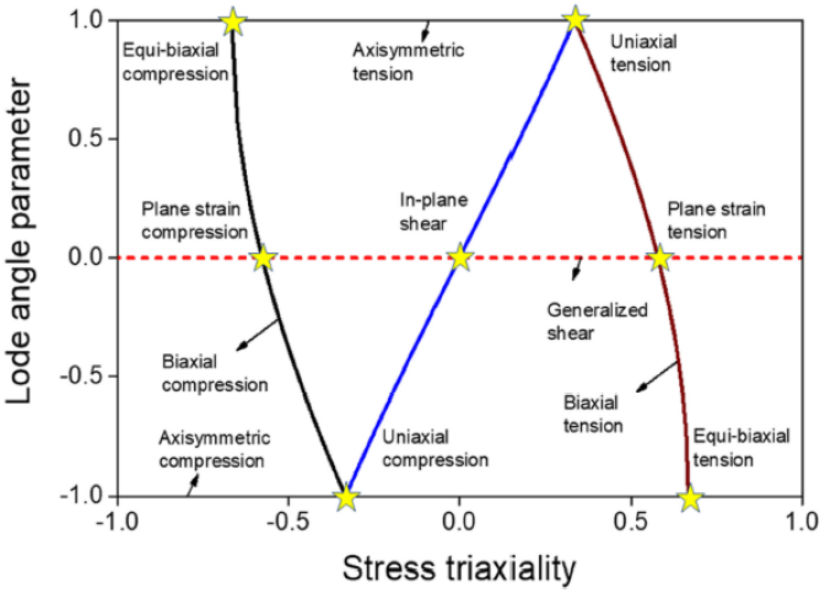

Figure 2.8: Stress states on the stress triaxiality and Lode angle parameter space [14]

For plane stress conditions, shown in the Figure 2.8 with the blue-black line, the Lode angle parameter may be expressed as a function of the stress triaxiality:

$$\bar{\theta} = 1 - \frac{2}{\pi} cos^{-1} \left(\frac{27}{2} \eta \left(\eta^2 - \frac{1}{3} \right) \right), \tag{2.12}$$

In other words, a single parameter η is sufficient to quantify the stress state under plane stress conditions. This is one of the reason why shell elements are preferred in the industry, since shell elements are implemented with the plane stress conditions. The Hosford-Coulomb criterion is described with the equation [10]:

$$\begin{aligned} \bar{\varepsilon}^{pr}_{HC}[\eta, \bar{\theta}] =& b(1+c)^{\frac{1}{n_f}} \\ & \times \left[\left\{ \frac{1}{2} \left((f_1 - f_2)^a + (f_2 - f_3)^a + (f_1 - f_3)^a \right) \right\}^{\frac{1}{a}} + c(2\eta + f_1 + f_3) \right]^{-\frac{1}{n_f}}, \end{aligned} \tag{2.13}$$

with the Lode angle dependent trigonometric functions:

$$f_1[\bar{\theta}] = \frac{2}{3} \left(\frac{\pi}{6} (1 - \bar{\theta}) \right), \tag{2.14}$$

$$f_2[\bar{\theta}] = \frac{2}{3} \left(\frac{\pi}{6} (3 + \bar{\theta}) \right), \tag{2.15}$$

$$f_3[\bar{\theta}] = -\frac{2}{3} \left(\frac{\pi}{6} (1 + \bar{\theta}) \right). \tag{2.16}$$

The model coefficient b is equal to the equivalent strain to fracture for equi-biaxial tension. The friction coefficient c controls the direct effect of the stress triaxiality, while the exponent a controls the indirect effect of the Lode angle parameter. The exponent $\mathrm{n_f} = 0.1$ is a material-independent transformation coefficient.

The material coefficients were obtained through curve fitting of experimental plastic strain at the onset of fracture for determined stress triaxiality levels. The Figure 2.9 illustrates the implemented workflow used for the calibration of the Hosford-Coulomb criterion. The input for the calibration was the fracture strain of three types of specimens, the UT, SHHD (shear high ductility specimen), and MN (mini Nakajima). The fracture strains were determined by comparing the force displacement curves and the DIC (digital image correlation) results. The experimental fracture strains were approximated using the Hosford-Coulomb law equation.

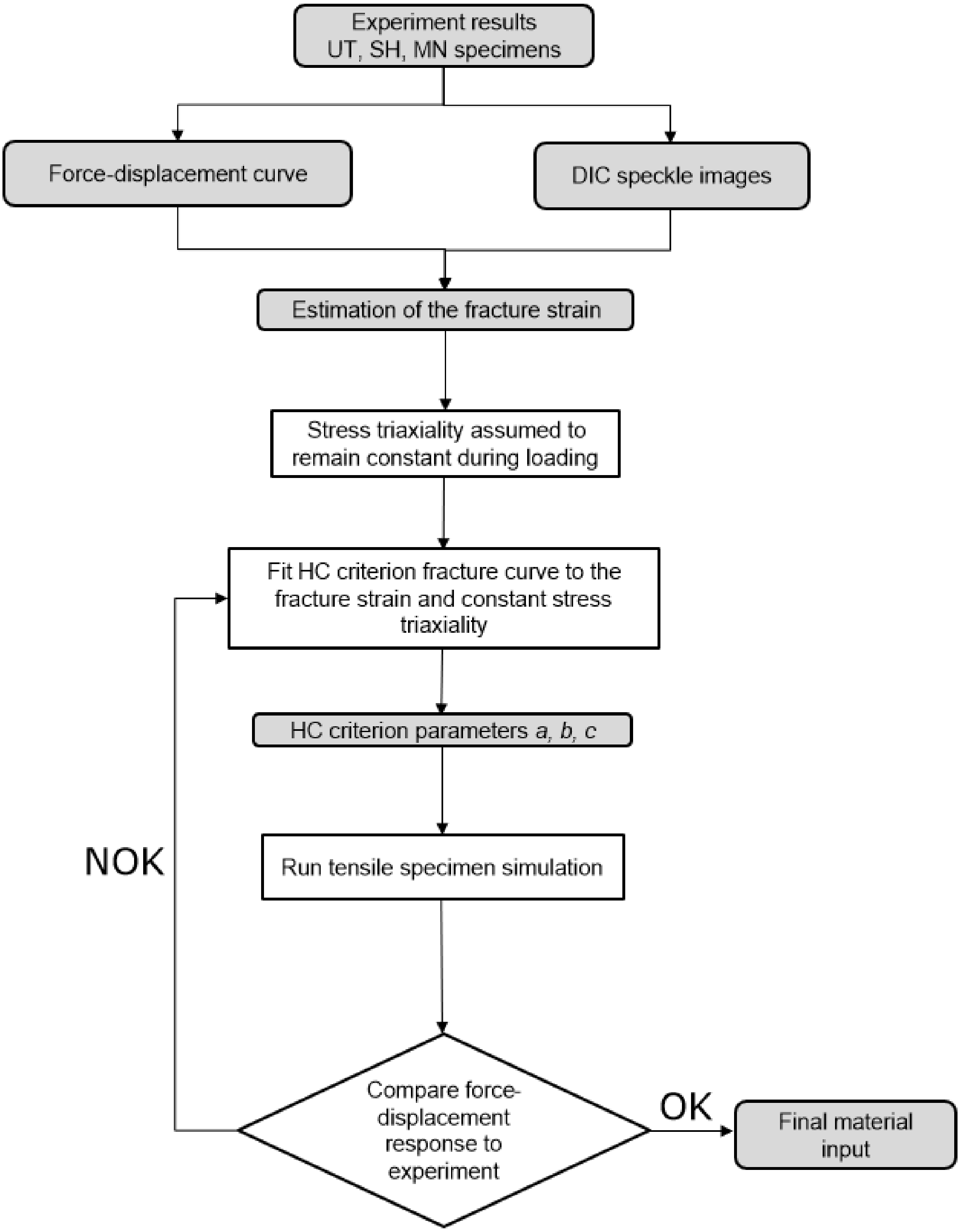

Figure 2.9: Hosford-Coulomb criterion coefficients determination workflow

3 Experimental procedure

3.1. Specimen geometry

To encompass a wide range of stress states, multiple geometries were employed for creating sheet metal specimens. Five types of tensile specimens were utilized to cover stress triaxiality ranging from 0.33 to 0.57, which includes the uniaxial tension to plane strain state. The selection of these geometries was based on previous research and the work of D. Mohr [15]. Three different types of shear specimens were chosen to cover the area of zero triaxiality. However, due to similar results, only one type was utilized for the numerical modelling. The selection of shear geometries was based on the study conducted by Roth and Mohr [16].

All specimens have the same thickness of 2.5 mm, and there very cut with a wire EDM (electrical discharge machining) to a tolerance within 0.01 mm. To consider the anisotropic properties of the aluminium alloy, the specimens were cut at different angles relative to the extrusion direction. In addition to the 0-degree orientation (along the extrusion direction), two additional angles were cut, namely 45 degrees and 90 degrees. The tensile specimens tested in this thesis are shown in Figure 3.1. The fist tensile specimen is UT specimen and the corresponding triaxiality in elastic region is constantly 0.33. Its gage section is 10 mm wide. The following two tensile specimen are made with the circular cut-outs of 20 mm and 6.67 mm radius, known as NT20 and NT6 respectively, and they cover triaxiality area from 0.4 to 0.57. These specimens are 20 mm wide but the notches reduce the width of the gage section to 10 mm in center. The last tensile specimen features a 20 mm wide gage section with an 5 mm diameter hole in the center, known as CH specimen (center hole).

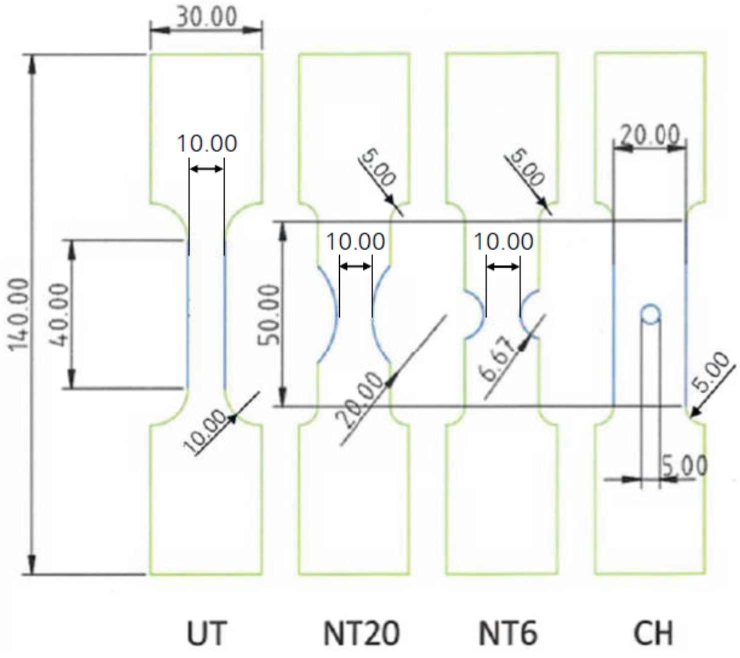

Figure 3.1: Tensile specimens geometry [19]

There are numerous shear test specimens which are suitable for different types of materials, shown in Figure 3.2. This topic is rather more complex but it wont be further discussed in this thesis.

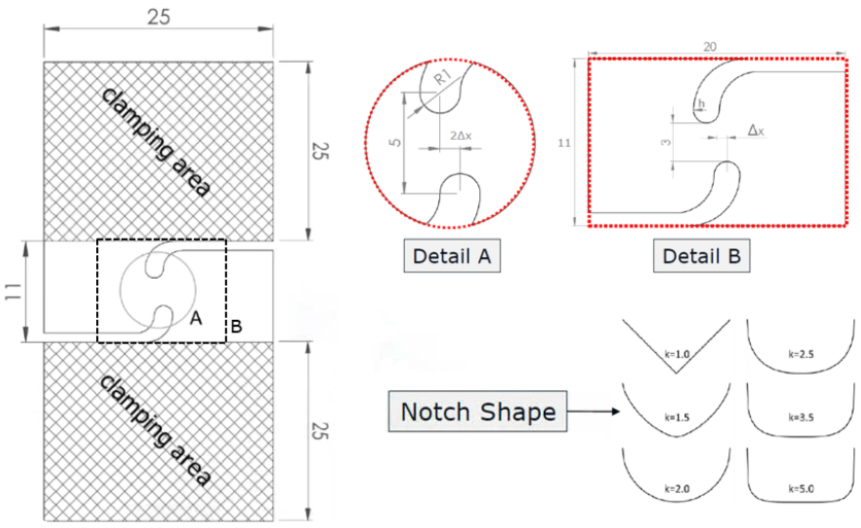

Figure 3.2: Shear specimens geometry [19]

Additional tensile specimen was used, the MN (Mini Nakajima) specimens. The Nakajima test specimens are a similar in idea to the punch test, the specimen (sample sheet) is clamped between the die and the blank holder while a punch punches through the middle of the specimen, as shown in the Figure 3.3

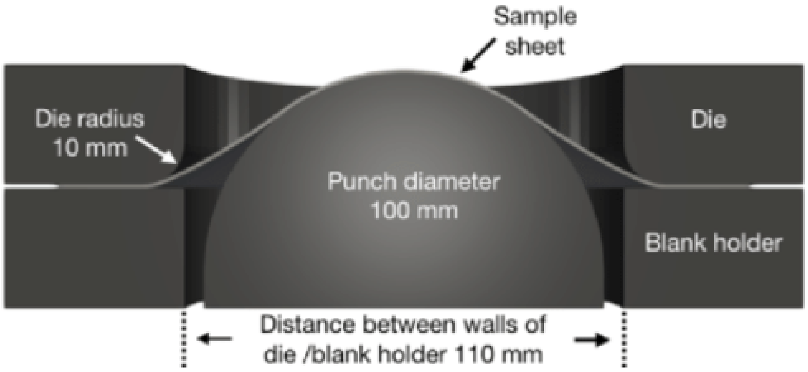

Figure 3.3: Experimental setup of the Nakajima test [17]

The Nakajima test is highly versatile, depending on the geometry of the specimen a wide range of stress triaxiality is achievable, which is ideal and necessary for the calibration of damage models. The Figure 3.4 shows the achievable stress states by changing the geometry of the specimen.

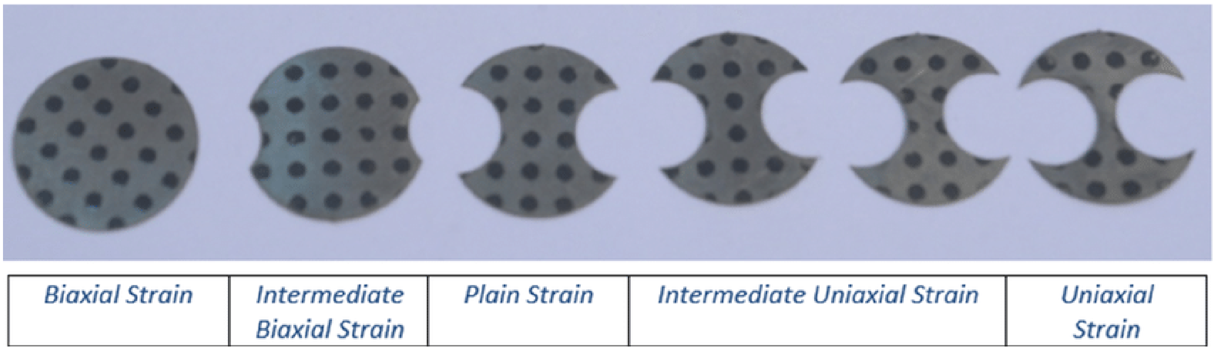

Figure 3.4: Nakajima test specimen [18]

The Mini Nakajima test is a modified version of the Nakajima test designed specifically for testing smaller specimens. Unfortunately, due to the timing of the results from the MN experiment, the simulation models were not prepared, and therefore, the MN test is not included in this thesis.

3.2. Experimental setup

ETH Zurich University conducted testing on both tensile and shear specimens. The universal tensile machine used for the experiments was the Inspekt 20-1, manufactured by Hegewald Peschke in Germany. The load cells of the machine provided direct force measurements for the tested specimens. To obtain displacement and strain fields, the VIC-2D software and the DIC (digital image correlation) method were used. The VIC-2D software used in this thesis was generously provided by *Correlation Studios*. The DIC method is a non-contact optical method that involves monitoring changes in point positions on the surface of the test sample. This is achieved by comparing the position of a measured point in the deformed state to its position in the undeformed state.

Prior to testing, a random speckle pattern was applied to the specimens to allow for the monitoring of point displacement. Digital images of the specimen surface were discretized into smaller subsets of facets, which formed a measuring volume of pixels. Each facet contained a central point that served as the measuring point for displacement and deformation results. The DIC method provided full displacement and strain fields on the surface of the specimen within the measuring volume. The experimental setup is shown in Figure 3.5.

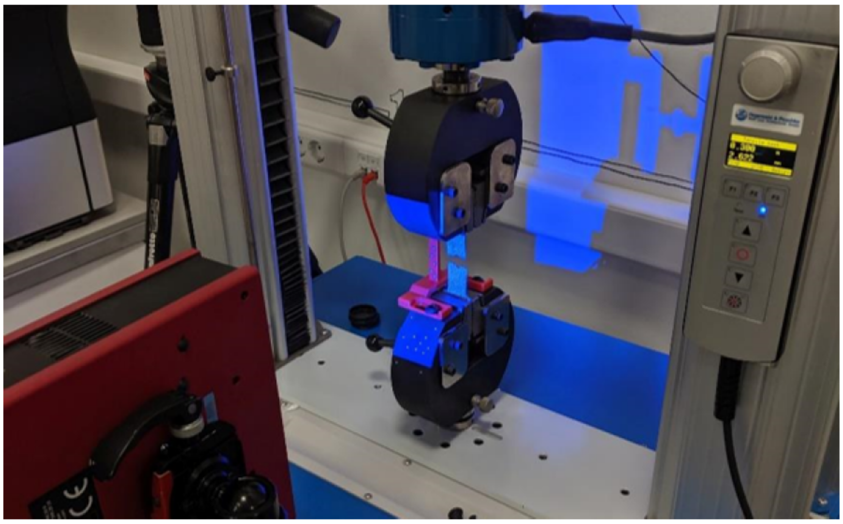

Figure 3.5: Measuring setup [19]

The tests were carried out under controlled conditions of 20 ± °C. To ensure a quasi-static response, a loading rate of 1 mm/min was used for all tests.

3.3. Experimental force-displacement results

In total, 75 specimens were tested, three tests per specimen geometry and at three different angles. UT specimens were additionally cut in four more angles, this was done to fine-tune the material anisotropic properties. Obtained result of four tensile specimens are shown in Figure 3.6.

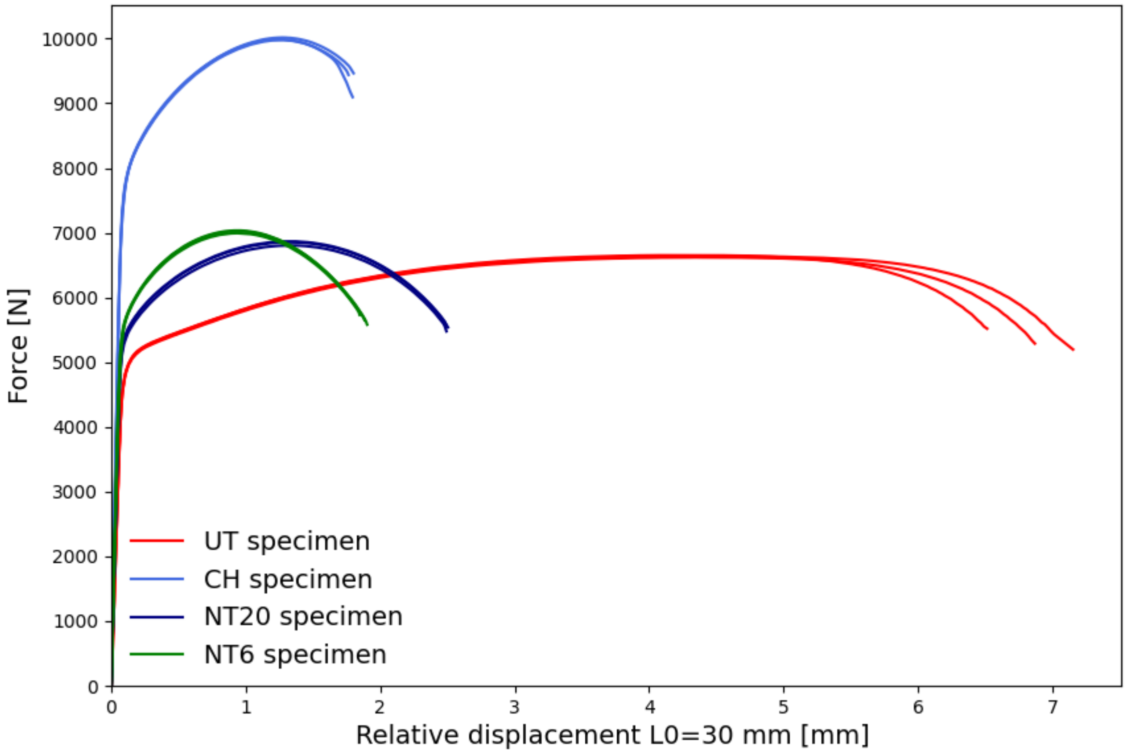

Figure 3.6: Force-displacements results of tensile specimens

Its important to highlight that the total force is measured by the tensile machine load cells, and the displacement is the relative displacement between two points 30 mm apart and its measured using the DIC method. It can be observed from the Figure 3.6 that the UT specimens display the greatest elongation before failure. All experiments reached a maximum force before fracture occurred, with the CH specimen demonstrating the highest force level. The force decrease between fracture initiation and failure was similar for the UT, NT20, and NT6 specimens, but fracture propagation was most pronounced for the CH specimens. There were no significant differences observed in the measured force-displacement results of each specimen type, indicating that test results were consistent and reliable.

In addition to tensile specimens, experiments with the shear specimens were also conducted. The samples were clamped and subjected to tensile loading, however due to the specimen geometry the fracture occurs under the shear stress state. As seen in the Figure 3.7, all three types of the shear specimens have similar response.

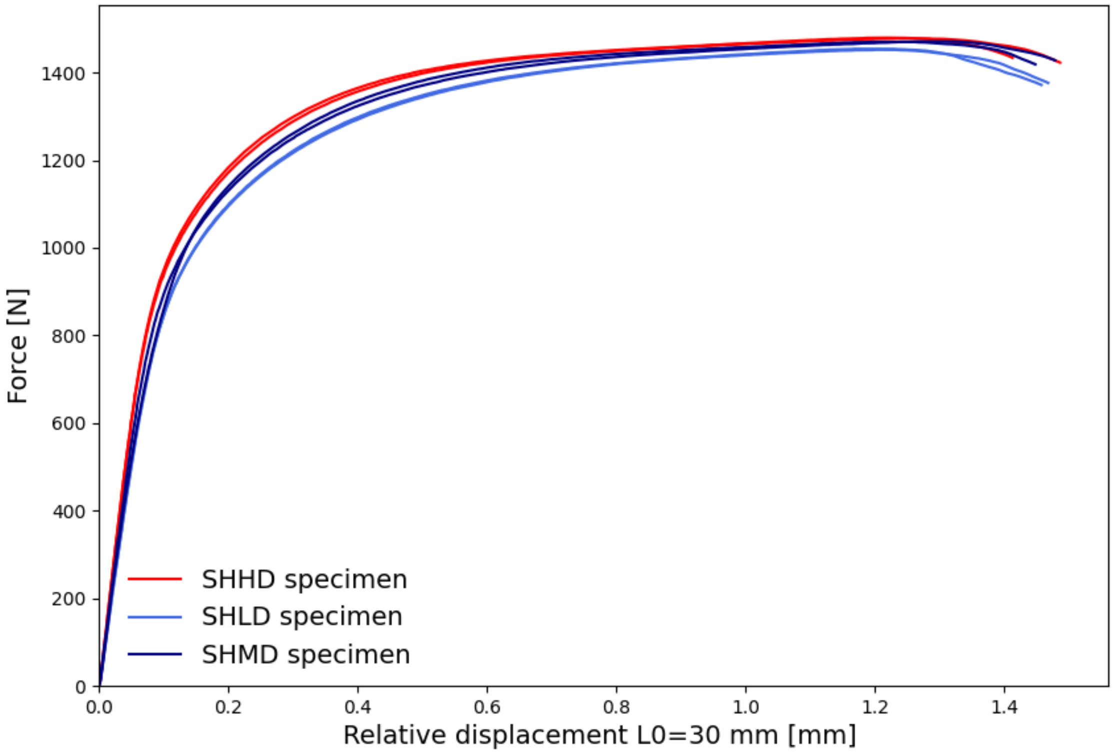

Figure 3.7: Force-displacements results of shear specimens

The highest achieved force is significantly smaller than in the tensile specimens. The force decrease after the fracture initiation and damage evolution is very pronounced for all shear specimens. Due to the similar response, the maximum force and displacement at failure were almost identical for all specimen types. Accordingly, only the SHHD shear specimen was used for the calibration of the material model.

4 Numerical calibration of Swift-Voce coefficients

4.1. Numerical quasi-static analysis

For the purpose of this research, finite element method (FEM) analysis was utilized. All simulation were run using the *Abaqus* software. All specimen geometries were discretized using the incompatible mode eight-node brick element (C3D8I), shown in Figure 4.1. This type of element has 8 nodes with 3 translation degrees of freedom (DOF) for each node, total 24 DOFs. Its an improved version of the C3D8 element. In particular, shear locking is removed and volumetric locking is much reduced [20]. Every specimen was prepared for numerical simulation in *Abaqus/Explicit* by using an *ANSA* pre-processor, which is widely used in the industry.

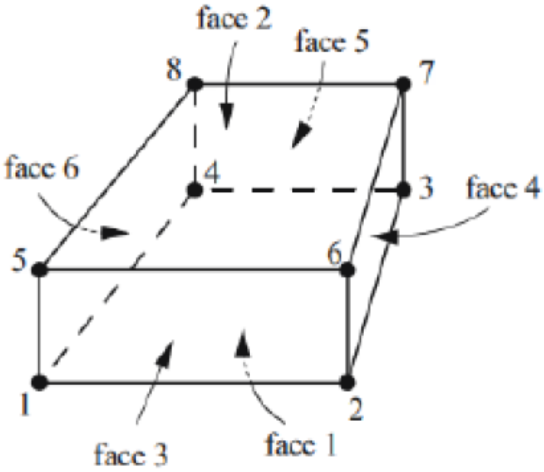

Figure 4.1: C3D8I element [20]

4.1.1. Quasi-static analysis using *Abaqus/Explicit*

Static, quasi-static, and dynamic are the three categories in which finite element method (FEM) analysis is commonly divided. When the problem involves deformation or load application at slow rates, a static analysis is recommended. For problems that require capturing high-frequency vibrations or impact loading, a dynamic analysis is more appropriate. In cases where there are significant nonlinearities or material failure, *Abaqus/Explicit* should be used for the analysis, while *Abaqus/Implicit* is best suited for problems that exhibit small to moderate nonlinearities. Explicit analysis is preformed in a large number of increments, the solution is determined without iterating by explicitly advancing the kinematic state from the previous increment. At the begging of the increment *Abaqus/Explicit* solves the dynamic equilibrium equation [20]:

$$M \cdot \ddot{u} = P - I, \tag{4.1}$$

where $\ddot{u}$ is the vector of nodal acceleration, M is the nodal mass matrix and P and I are respectively the vector of external forces and the vector of internal element forces. The vector of nodal accelerations at the beginning of the increment (time i) is calculated from the equation:

$$\ddot{u}|_{(i)} = M^{-1}(P - I)|_{(i)}. \tag{4.2}$$

The nodal velocities at the middle of the current stable time increment Δt are calculated by accelerations integration through time using the central difference rule, and addition to the velocity at the middle of the previous increment:

$$\dot{u}|_{(i+\frac{1}{2})} = \dot{u}|_{(i-\frac{1}{2})} + \frac{\Delta t|_{(i+1)} + \Delta t|_{(i)}}{2} \cdot \ddot{u}|_{(i)}. \tag{4.3}$$

The calculated nodal velocities are integrated and through time and added to the displacements at the beginning of the increment to obtain the nodal displacements at the end of the increment:

$$u|_{(i+1)} = u|_{(i)} + \Delta t|_{(i+1)}\dot{u}|_{(i+\frac{1}{2})}. \tag{4.4}$$

The state at the end of the increment (i + 1) is based solely on the displacements, velocities, and accelerations at the beginning of the increment (i). This approach assumes that accelerations are constant during an increment, so in order to produce the accurate results, the time increment must be rather small. Tor this reason the analyses usually require a large number of increments. However, each increment is computational inexpensive because there are no simultaneous equations to solve. The key to the computational efficiency is the use of diagonal and lumped nodal mass matrix M. This results in uncoupled equations of motion and therefore no tangential stiffness calculation is required for explicit analysis. Furthermore, the inversion of M is trivial, which reduces the time cost of the analysis.

The size of the increment, in which the state can be advanced and still remain an accurate representation of the problem, is limited by the stability factor. The stability limit can be estimated with the following expression:

$$\Delta t \approx \frac{L_{min}}{c_d}, \tag{4.5}$$

where L_{min} represents the smallest element dimension and c_d represents the dilatational wave speed. The shorter the element length, the smaller the stability limit. The dilatational wave speed is the material property and its calculated using the equation:

$$c_d = \sqrt{\frac{E}{\rho}}, \tag{4.6}$$

where ρ is the density and E the Young's modulus. This effectively means that the time increment can be no larger than the stability limit, more precisely the time required to propagate a stress wave across an element [20].

Special attention is needed when using *Abaqus/Explicit* to simulate quasi-static phenomena. It is computationally impractical to model the process in its natural time period, the analysis would take too long to be practical. The speed of the process in the simulation is artificially increased to obtain an economical solution, however its important to preserve negligible inertial effects. The simulation time can be shorted by increased load rates and/or mass scaling. Increased load rates reduces the time scale of the simulation, so fewer increments are needed to complete the job. Mass scaling artificially augments the material density to increase the stable time increment. To preserve the quasi-static phenomena, it is essential to preform an energy control, where the ratio of kinetic to internal energy must not exceed 10% throughout the analysis. Consequently, the work done by the external applied loads is approximately equal to the internal energy of the system through the analysis.

4.1.2. Numerical model

Every specimen geometry was prepared in *ANSA* pre-processor to represent the conditions of the experiment. As all the tensile models exhibit triaxial symmetry, computational time was saved by modelling only 1/8 of the specimen geometry. The same approach used for the tensile models could not be applied to the shear specimens. Instead, only the thickness symmetry was exploited. To improve visualization, the Figure 4.2 includes full models without symmetry for better clarity. Three symmetry boundary condition were applied to the models, symmetry around the YX, XZ, and ZY plane. For the shear specimens only the symmetry around the XY plane was applied. Two reference points were defined in the models: the first reference point represented the lower clamping zone, where all degrees of freedom were fixed, and the second reference point represented the upper clamping zone, where the displacement load in the extrusion direction was applied, while all other degrees of freedom were fixed.

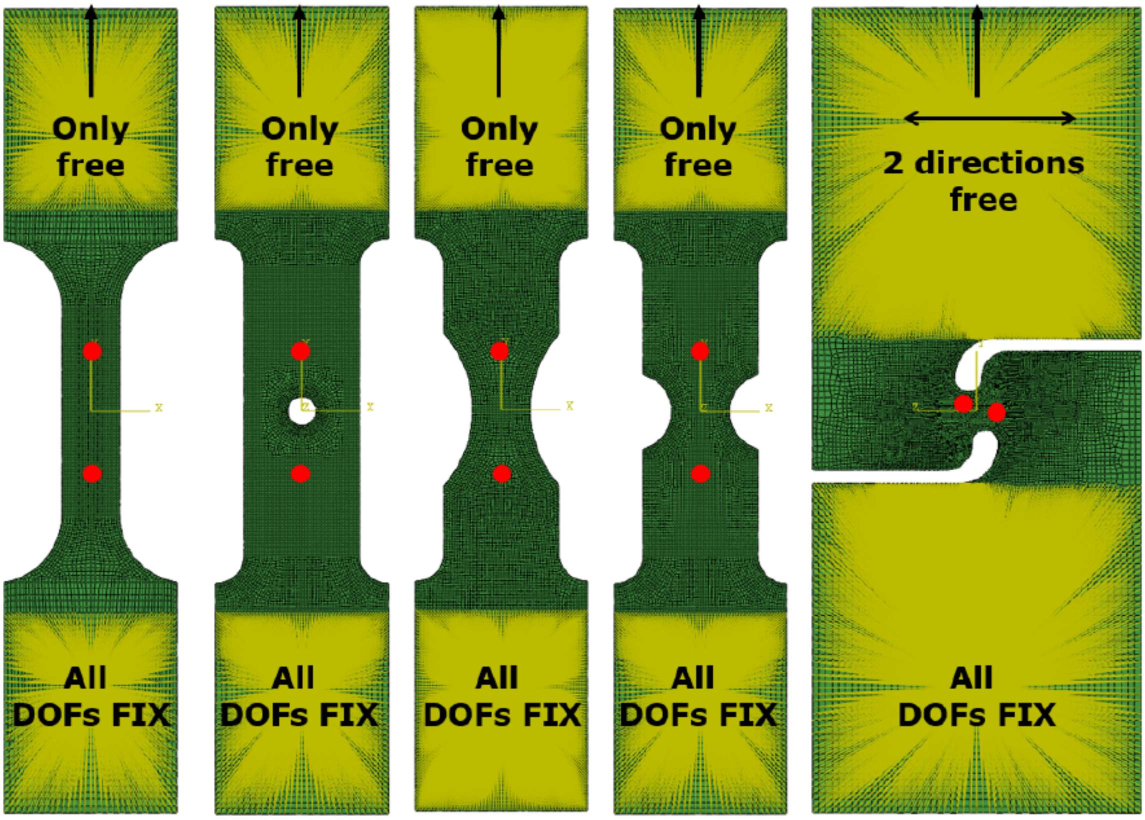

Figure 4.2: Numerical models

The reaction force data was obtained from the fixed reference point. The relative displacement was obtained with a displacement extraction node, +15 mm from the model center, and its marked with a red dot in Figure 4.2. An element size of 0.01 mm was chosen, that gives 8 elements though the thickness.

4.2. Swift-Voce hardening calibration

The calibration process used for the parameter determination is shown in Figure 4.3. Based on the experimental results obtained from the UT specimen, the force-displacement curves can be extracted and used to calculate the engineering stress-strain curve. Afterwards, the engineering stress-strain data is recalculated into true stress-strain data up to UTS (ultimate tensile stress). Figure 4.3 displays both the engineering stress-strain and true stress-strain curves.

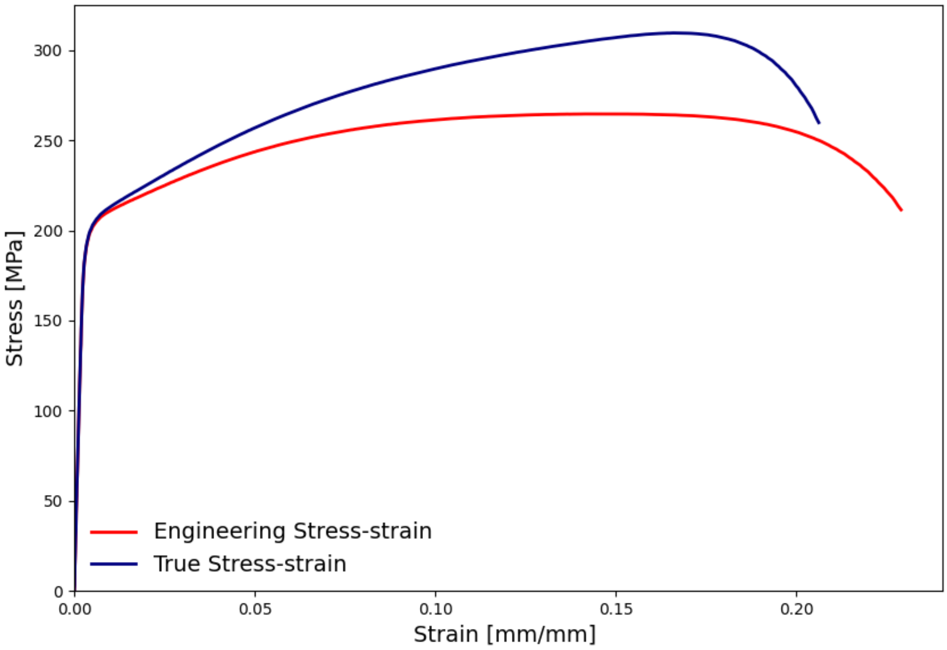

Figure 4.3: Engineering and true stress-strain curves

Since the Swift and Voce hardening parameters are determined from true stress-plastic strain curves, the elastic strain component needs to be subtracted from the total true strain. The resulting true stress plastic strain curves is shown in Figure 4.4.

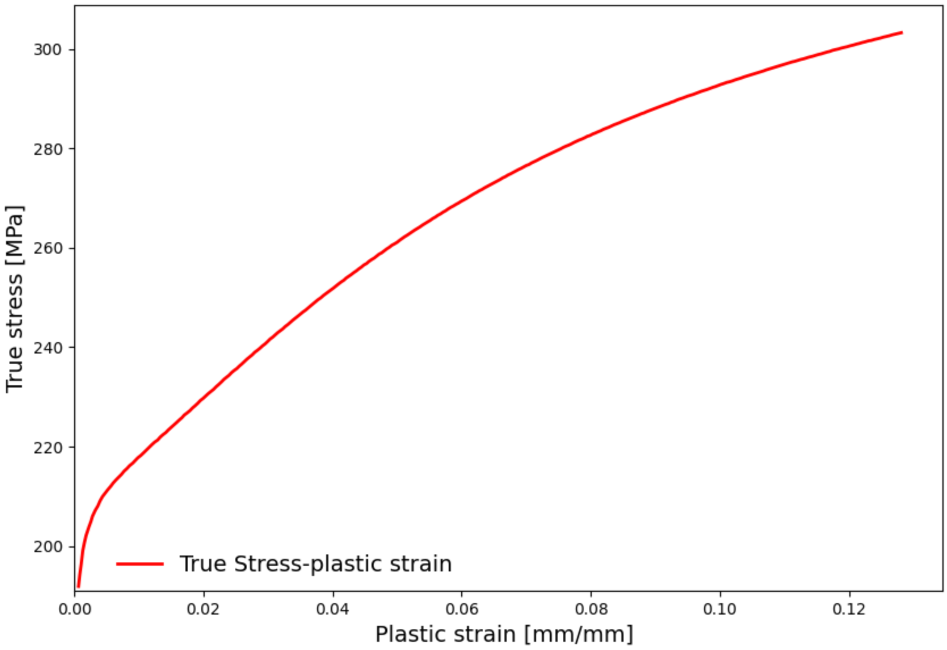

Figure 4.4: True stress-plastic strain curve

The curve shown in the Figure 4.4 represents the average value obtained from three UT speciments test and its used for the hardening calibration. The Swift and Voce hardening parameters are obtained from a least-square fit algorithm using the *Python* software. The parameters obtained are shown in Table 4.1.

Table 4.1: Swift and Voce hardening coefficients obtained by curve fitting

Swift coefficients	A [MPa]	451.056
	ε_0 [-]	0.0163
	n [-]	0.2012
Voce coefficients	k_0 [MPa]	200.775
	Q [MPa]	126.169
	β [-]	13.169

The weighting factor α determines the influence of each flow law in the final hardening curve and plays an important role in the post-necking range. According to [19] is determined through inverse analyses using the simulations in *Abaqus*. However, the initial calibration of α using simple curve fitting gave a satisfying result, and further calibration wasn't deemed necessary. The value weighting factor α is shown in the table

Table 4.2: The weighting factor α

α [-]	0.225

The value of the weighting factor indicates that the Swift hardening law has the dominant role in the final hardening curve. The calibrated Swift, Voce, combined Swift-Voce hardening laws, and the true stress-plastic strain are shown in Figure 4.5. Its visible that Swift law exhibits saturation at high plastic strains, while Voce law does not. At low plastic strains the two hardening laws overlap.

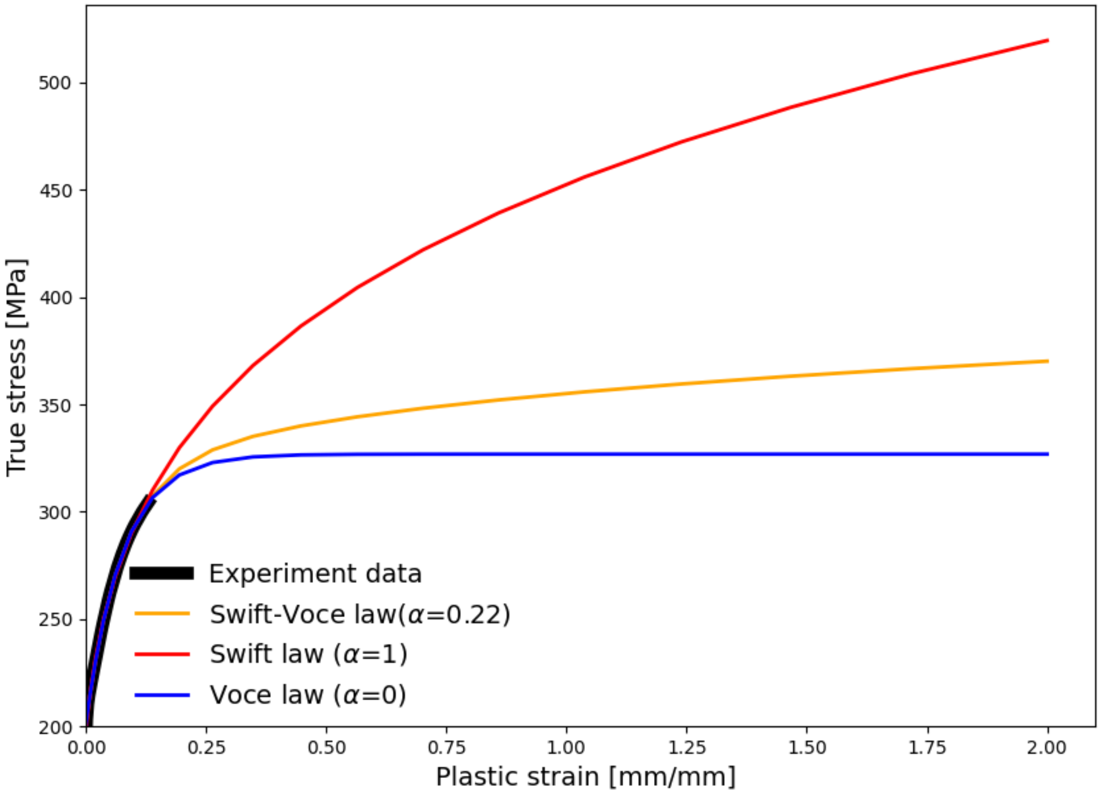

Figure 4.5: Swift, Voce, and combined Swift-Voce hardening laws

4.2.1. Force-displacement response

The figures below show force-displacement response obtained from measurements and simulations. The results show that the proposed Swift-Voce hardening model is effective in predicting the load-displacement relation for all specimens.

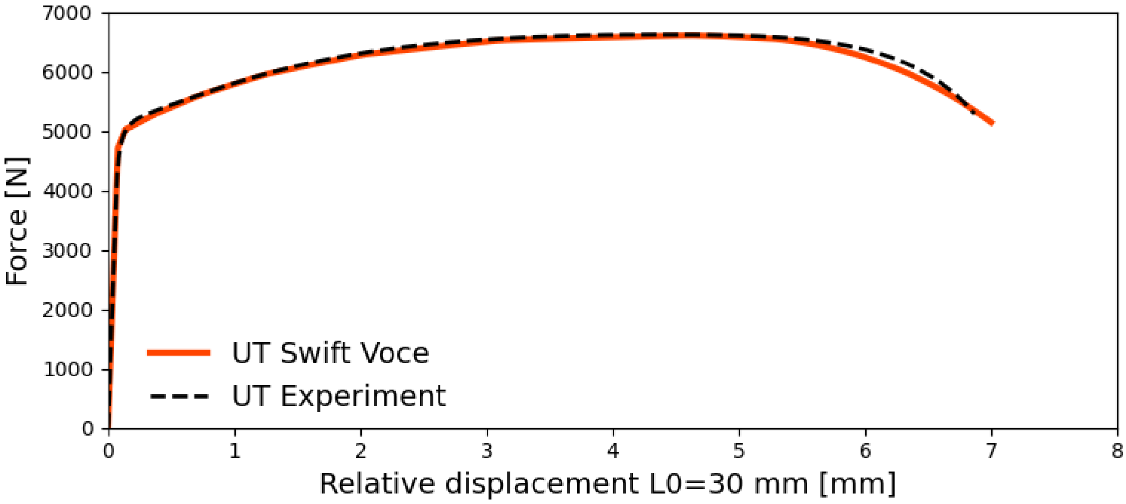

Figure 4.6: Force-displacement response of UT specimen

The response of the simulated UT specimen shown in Figure 4.6 matches well with the experiment.

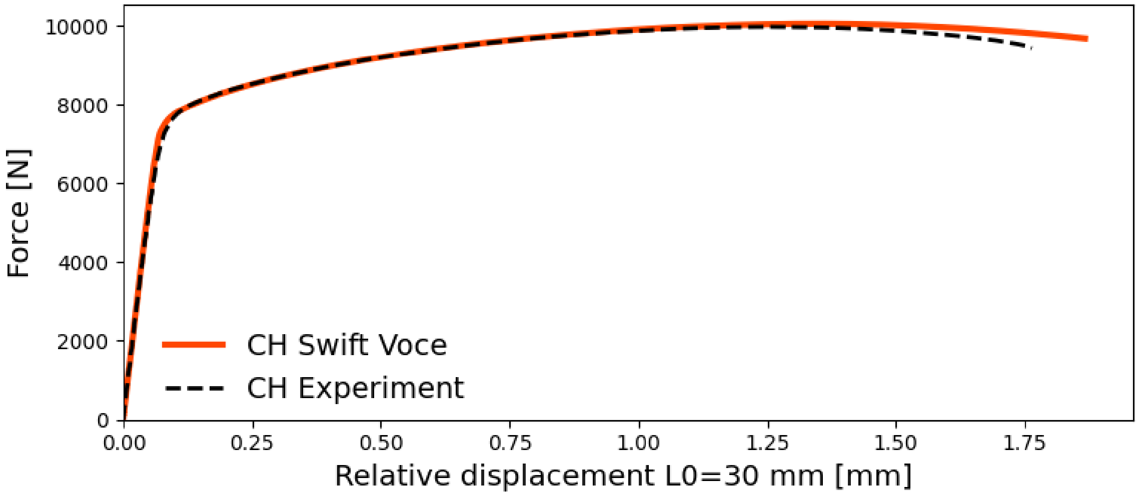

Figure 4.7: Force-displacement response of CH specimen

The simulated CH specimen, as depicted in Figure 4.7, exhibits a good match with the experimental results.

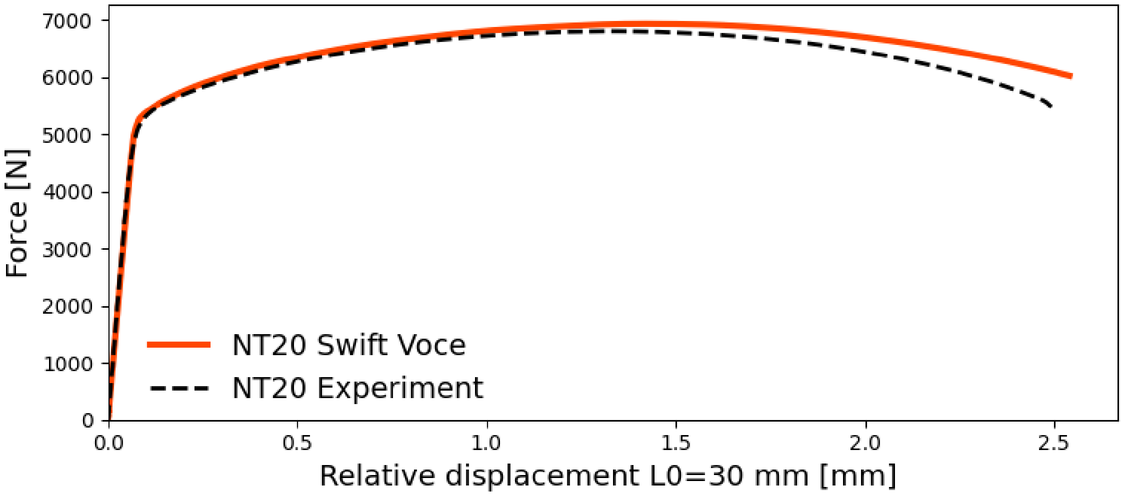

Figure 4.8: Force-displacement response of NT20 specimen

The simulated NT20 specimen shown in the Figure 4.8 shows a slight underprediction of the maximum force when compared to the experimental results. The simulated force-displacement curve follows closely the experimental curve only up the point of UTS.

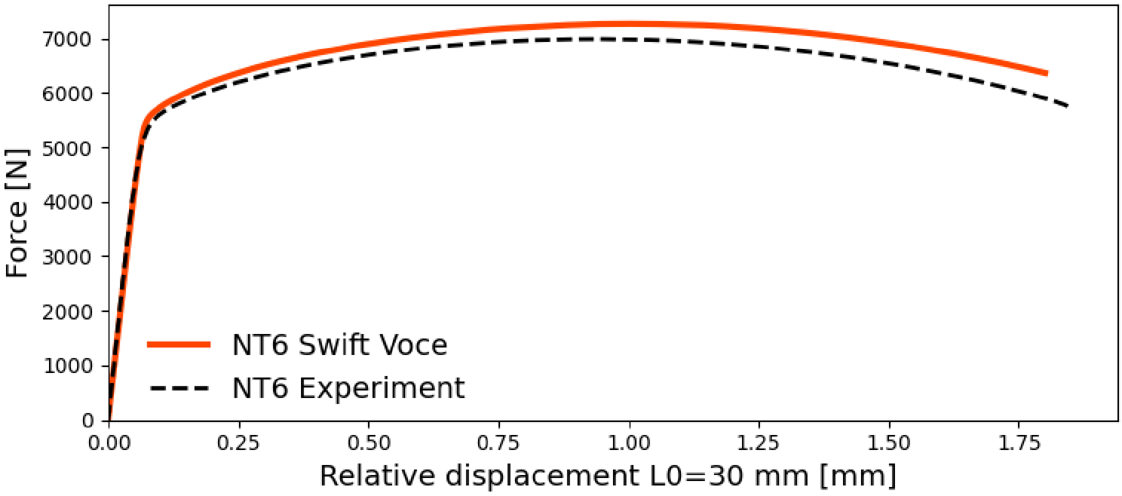

Figure 4.9: Force-displacement response of NT6 specimen

The simulated NT6 specimen shown in the Figure 4.9 shows a greater underprediction of the maximum force. The underprediction of the maximum force in both specimens, NT20 and NT6, was caused by the same factor. Due to the anisotropy of extruded material, the mechanical properties in non-extrusion direction are weaker. Due to specific geometry, the stress values are high in non-extrusion direction for these specimen types. The proposed Swift-Voce model uses the von Mises yield surface in combination with isotropic hardening, and therefore, it can not adequately capture this effects.

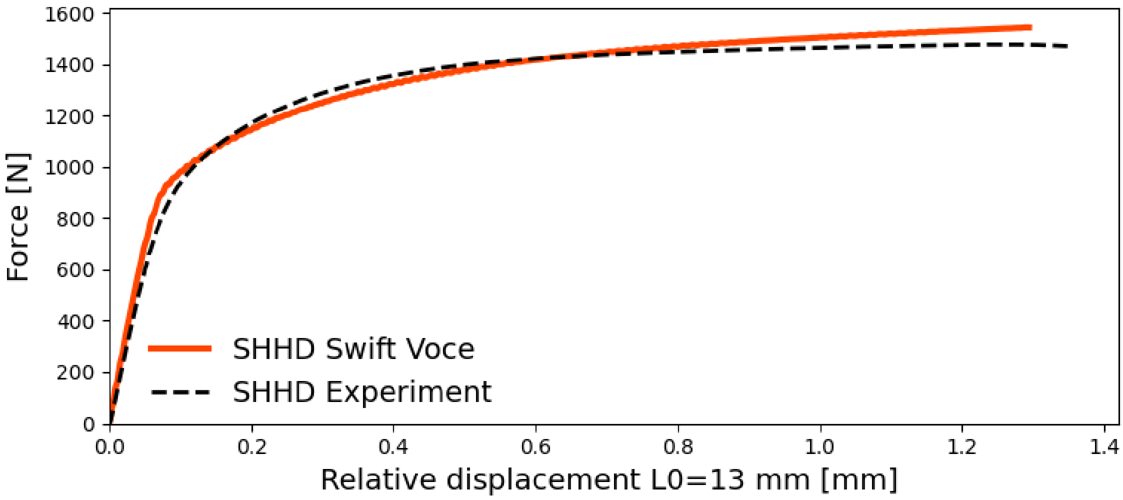

Figure 4.10: Force-displacement response of SHHD specimen

The simulated SHHD specimen shown in Figure 4.10 exhibits good agreement with the experimental data, due to the similar response of all three shear specimens, only the SHHD specimen is presented.

In general it can be concluded that the calibrated combined Swift-Voce hardening law correctly predicts the material force-displacement response, however there is anisotropy present in the material that can be clearly seen in the NT20 and NT6 specimens.

5 Numerical calibration of anisotropic coefficients

5.1. Hill 48 and Barlat Yld2000 yield calibration

The calibration process used for the coefficients determination is shown in Figure 5.1. Based on the experimental results obtained from the UT specimen, the stress and Lankford ratios can be extracted at their saturated values, shown in Figure 5.1, and used to calibrate the anisotropic yield criterion.

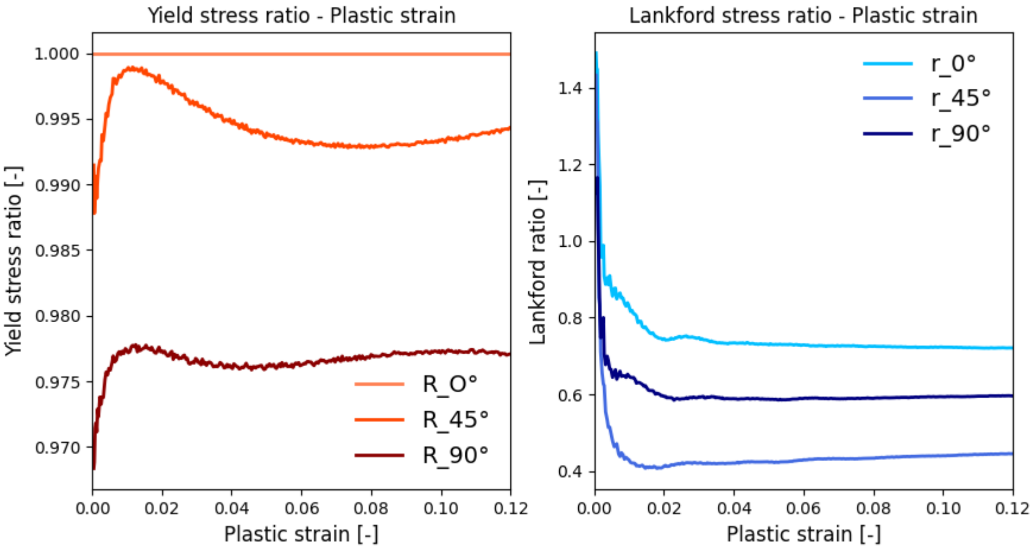

Figure 5.1: Experimental stress and Lankford ratios

The Hill 48 and Barlat Yld2000 coefficients are obtained from a least-square fit algorithm using the *Python* software. The coefficients obtained are shown in Table 5.1.

Table 5.1: Hill 48 and Barlat Yld2000 coefficients obtained by curve fitting

Barlat Yld2000 Coefficients	a_1	0.9724	a_5	0.9900
	a_2	0.9650	a_6	0.8613
	a_3	0.9210	a_7	0.9267
	a_4	1.0240	a_8	1.1707
Hill48 Coefficients	F	0.6280	H	0.4286
	G	0.5708	N	1.449

The measured and calculated stress and Lankford ratios are shown in Figure 5.2. It can be observed that both models predict the stress ratio accurately. However, the Hill 48 model fails to predict the Lankford ratio correctly.

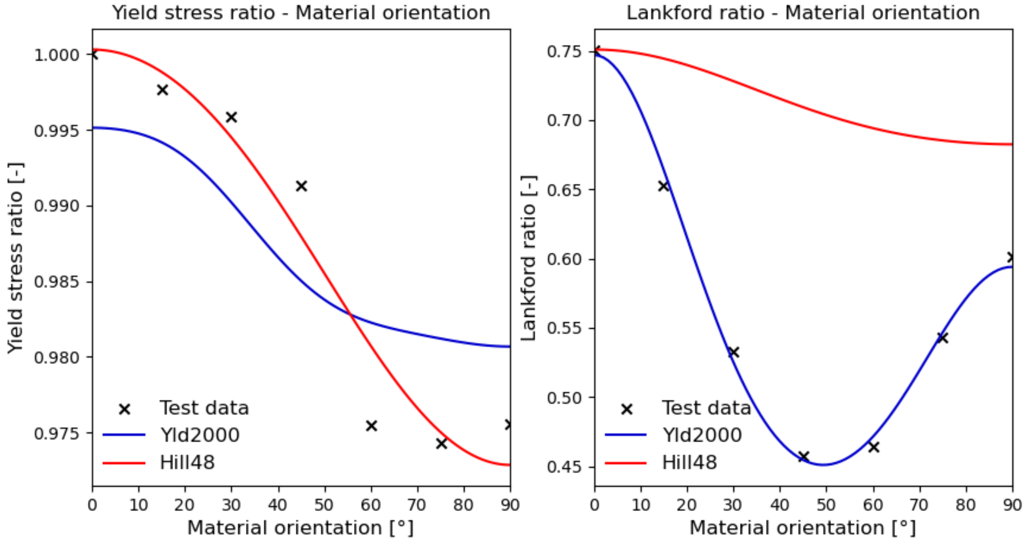

Figure 5.2: Hill 48 and Barlat Yld2000 anisotoropic yield models

5.1.1. Force-displacement response

The figures below show force-displacement response obtained from measurements and simulations. The results compare the von Mises isotropic yield, as well the Hill 48 and Barlat Yld2000 anisotropic yield models. The plastic hardening law is kept the same, the combined Swift-Voce hardening law. It should be noted that the implementation of anisotropic yield models led to a significant prolongation of the simulation time. Despite utilizing the same number of CPUs, the simulation duration increased from 20 minutes to 70 minutes for identical models with the same number of elements. This increase in simulation time becomes more significant when dealing with more complex models commonly employed in the industry. To visualize the material anisotropy the specimens were cut in three orientations to the extrusion direction, and accordingly three simulation per specimen were run with different material orientation.

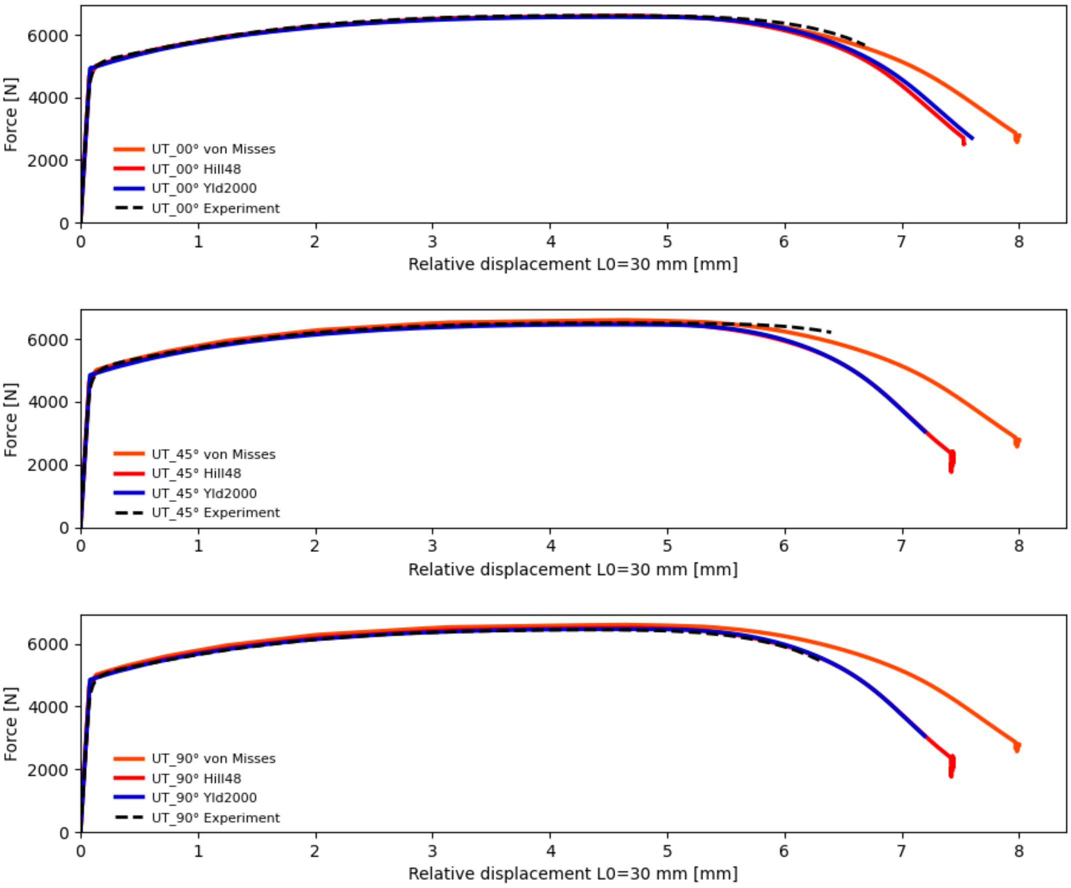

Figure 5.3: Force-displacement response of UT specimen for the 0°, 45°, and 90° orientation

The response of the simulated UT specimens shown in Figure 5.3 match well with the experiments, it can be observed that all material models overlap until the UTS point after with they diverge. The alloy is the strongest in the 00° orientation, in the direction of the extrusion while it is the weakest in the 90° orientation, perpendicular to the extrusion direction. It can be seen that for the 90° orientation the von Misses yield model expectedly overpredicts the total force after UTS. Both models have proven to be effective in capturing the anisotropic nature of the material. Although, as noted earlier, the material's anisotropic properties are not pronounced in the UT specimen, other specimens geometries should serve as a benchmark to evaluate the anisotropic yield models.

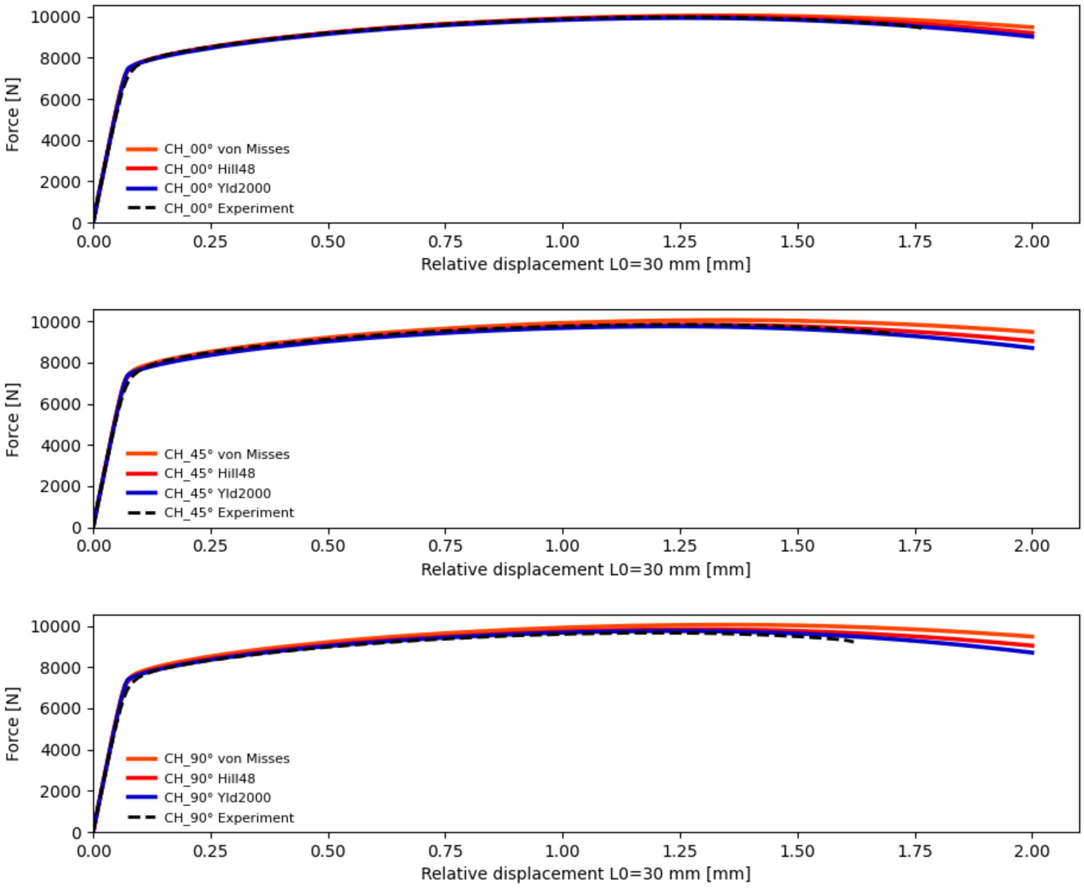

Figure 5.4: Force-displacement response of CH specimen for the 0°, 45°, and 90° orientation

The simulated response of the CH specimen, depicted in Figure 5.4, behaves in a similar manner as the UT specimen. All material models exhibit a good agreement until the UTS point, beyond which they start to diverge, the biggest difference is seen in the 90°

orientation.

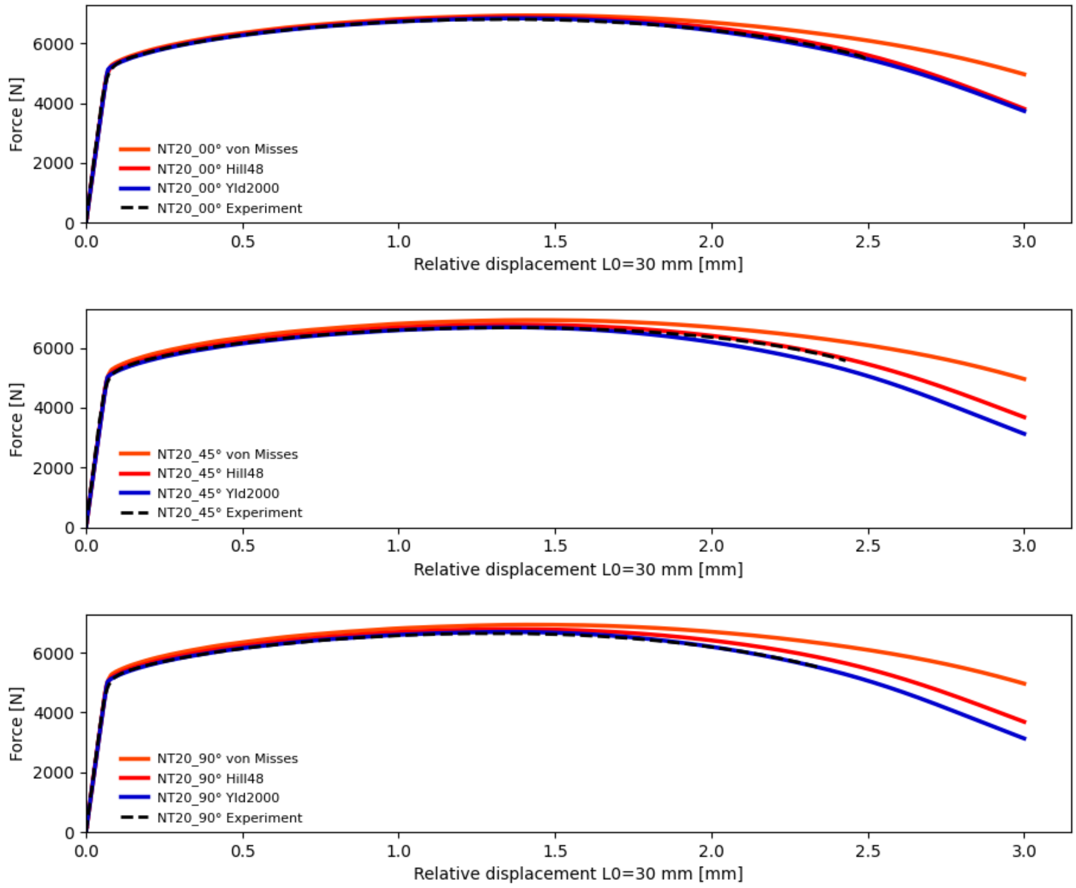

Figure 5.5: Force-displacement response of NT20 specimen for the 0°, 45°, and 90° orientation

The simulated NT20 specimen shown in the Figure 4.8 shows a greater mismatch between isotropic and anisotropic models after the UTS point.

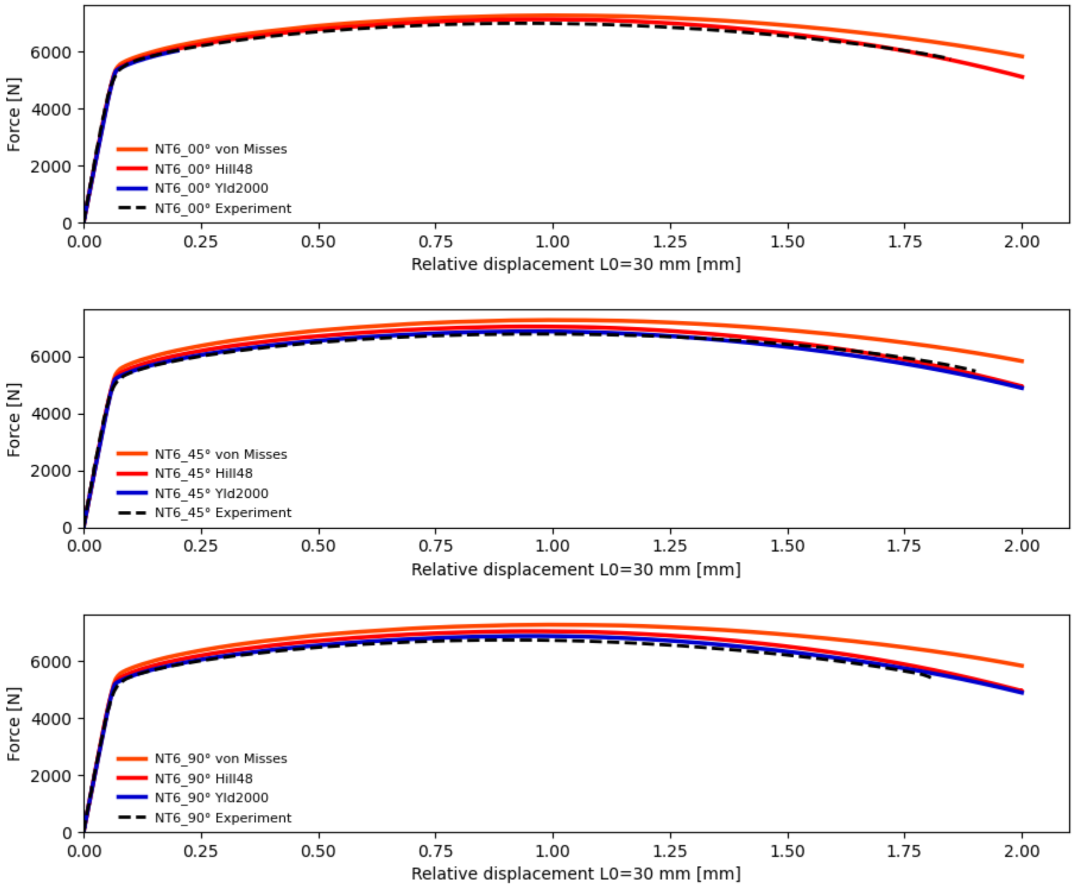

Figure 5.6: Force-displacement response of NT6 specimen for the 0°, 45°, and 90° orientation

It can be seen from the Figure 4.9 that the experimental and simulated response of the NT6 specimen behave differently to all other specimens. In the other specimens all curves would overlap up to the UTS point, and after the maximum force was reached they would diverge. In this case, for the 45°, and 90° orientation the entire experimental force- displacement curve is offset. The von Misses model fails to capture this, the simulated force level is almost 15 % above than the experimental force response. The force-displacement response is well captured by both anisotropic models.

Shear specimens were treated with special care. In order to capture the shear failure of the material a fine and structured mesh was used. Another issue encountered in the simulation of the shear specimens was a very noisy output. All simulation were run with a fixed time increment of one millisecond, the simulation time was shorted through use of mass scaling. After each simulation, the energies were carefully examined to ensure that the results were physically meaningful and valid. However, this approach did not work well with the shear specimens, and it was necessary to shorten the fixed time increment to half of a millisecond, which doubled the simulation time. On a high-performance computing server with 128 central processing units (CPUs), the simulation time was approximately 2.5 hours.

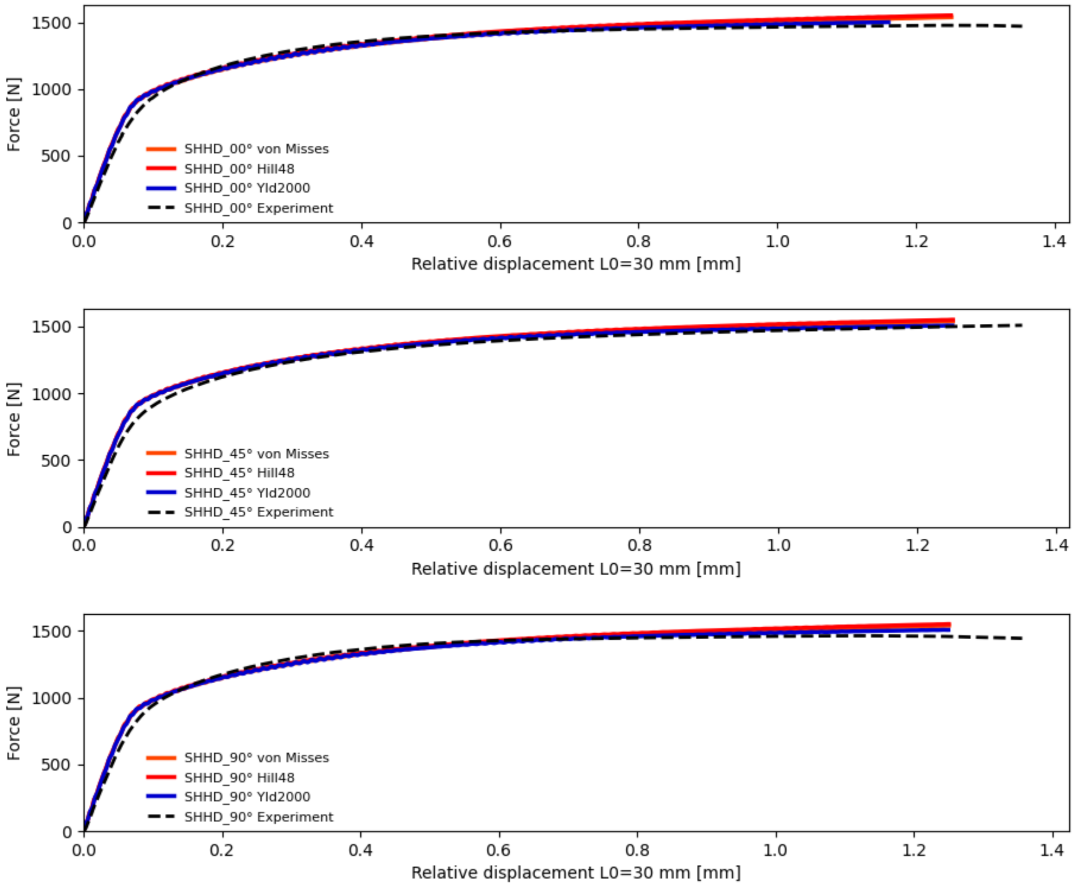

Figure 5.7: Force-displacement response of SHHD specimen for the 0°, 45°, and 90° orientation

All simulated SHHD specimen shown in Figure 5.7 exhibits good agreement with the experimental data.

6 Numerical calibration of Hosford-Coulomb criterion parameters

6.1. Hosford-Coulomb criterion calibration

Figure 2.9 illustrates the implemented workflow used for the calibration of the Hosford-Coulomb criterion. The plastic strain at the onset of fracture is estimated using the VID-2D software and the DIC method. The UT, SHHD, and MN specimens were used for the calibration, The extraction points of the fracture strain are shown in Figure 6.1.

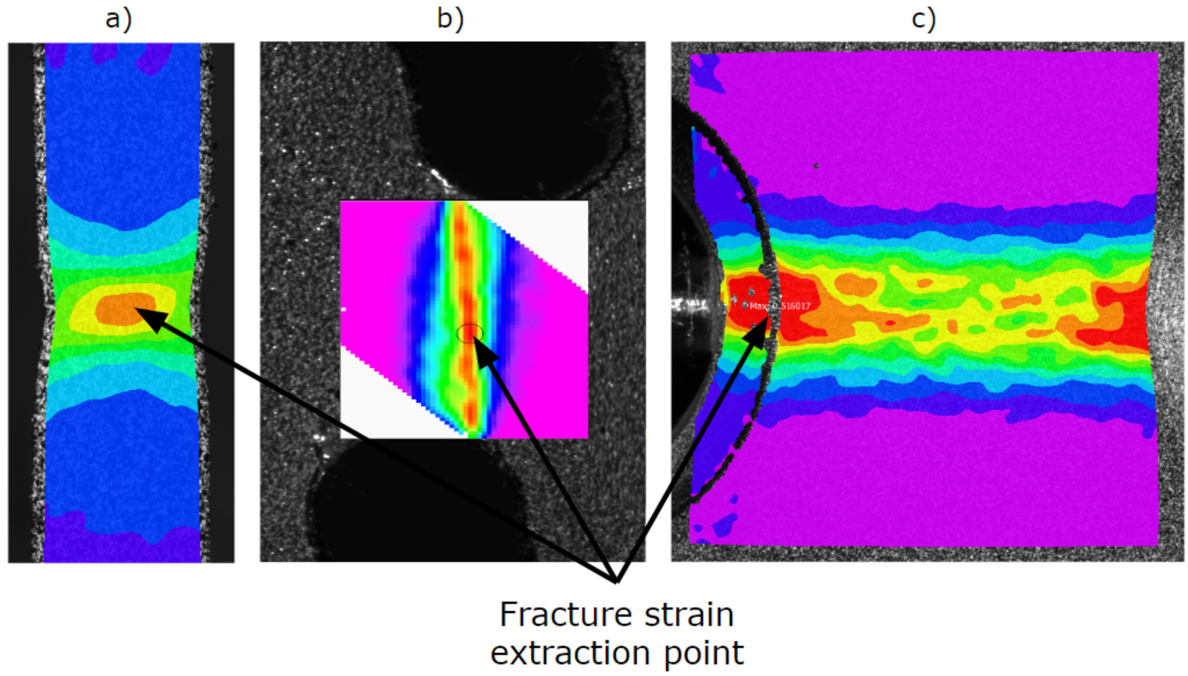

Figure 6.1: Plastic strain extraction points for: a) UT specimen, b) SHHD specimen, c) MN specimen

The determination of the exact fracture initiation point, as well as the exact initiation moment is almost impossible. Therefore, the fracture initiation displacement in this thesis is regarded as the point where the load is reduced sharply in the experiment. The obtained experimental fracture strain and corresponding triaxiality levels at the beginning of the loading step are displayed in Table 6.1.

Table 6.1: The equivalent plastic strain and stress triaxiality at the onset of damage

	Plastic strain [-]	Triaxiality [-]
SHHD	1.04	0
UT	0.51	0.33
MN	0.37	0.58

For the purpose of this thesis, the stress triaxiality is assumed to remain constant during the loading step. This assumption is critical for the following steps and allows for a fast calibration of the damage model. A more detailed and time-consuming way to calibrate the damage model would be to obtain the triaxiality path to fracture using the numerical simulations without any implemented damage model. The equivalent plastic strain and stress triaxiality would be extracted at the integration point of the element with the highest equivalent plastic strain. This thesis investigates whether a fast calibration of the Hosford-Coulomb criterion would yield acceptable results. For this reason, the UT, SHHD, and MN specimens were selected, as they exhibit minimal variations in triaxiality across the all specimen types.

The Hosford-Coulomb criterion parameters are obtained from a least-square fit algorithm using the *Python* software. The parameters obtained are shown in Table 6.2.

Table 6.2: Hosford-Coulomb coefficients obtained by curve fitting

HC coefficients	a [-]	1.67
	b [-]	0.51
	c [-]	0.09

The calibrated fracture locus in the equivalent plastic strain and stress triaxiality space is shown in Figure 6.2. Additionally, three fracture points used for the calibration can be observed as well.

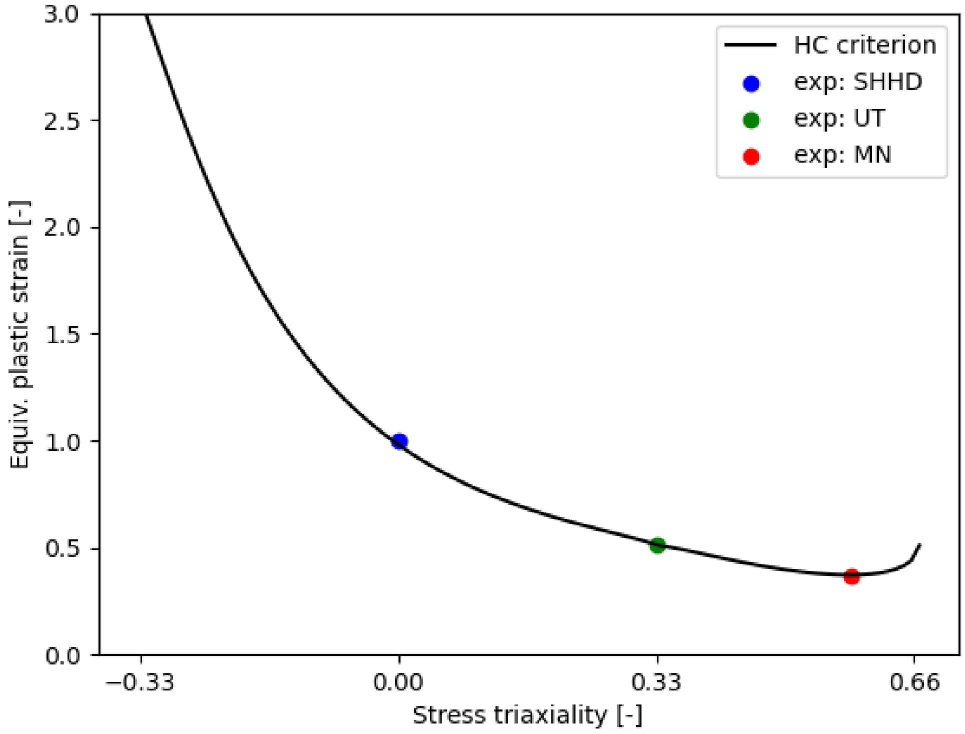

Figure 6.2: Calibrated fracture locus in the equivalent strain and stress triaxiality space

6.1.1. Force-displacement response

The figures below show force-displacement response obtained from measurements and simulations. Due to the overwhelming number of required simulations for all possible options, encompassing five specimens, three material orientations, and two anisotropic models, only one representative simulation will be shown to provide a concise overview. Considering the rather small impact of the anisotropic effects, only the isotropic models with the implemented HC criterion are shown. While acknowledging that this is a simplification, it is a more useful comparison for industrial applications, since determining the material orientation for complex components can be highly time-consuming and sometimes even impossible.

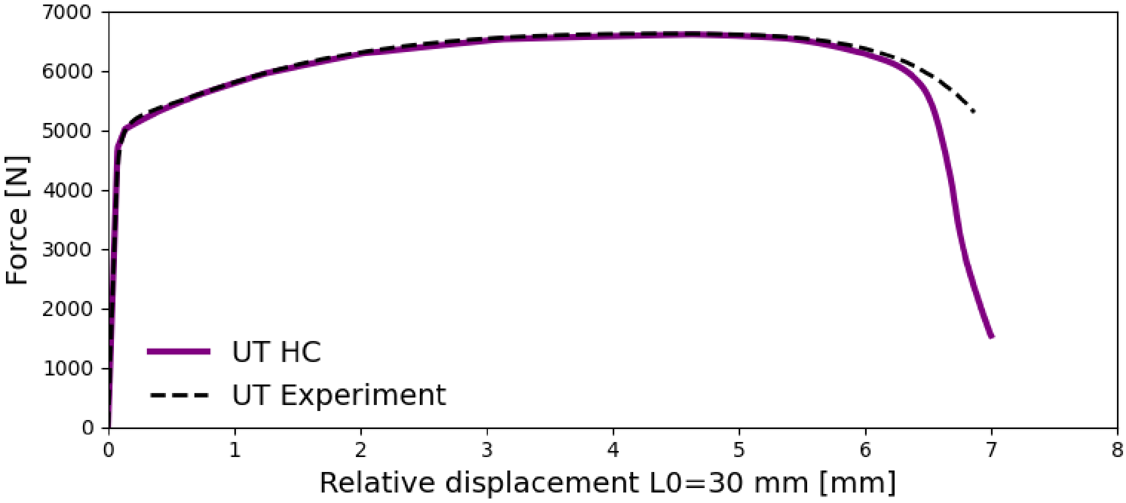

Figure 6.3: Force-displacement response of UT specimen

The response of the simulated UT specimens shown in Figure 6.3 match well with the experiments. Additionally, it can be seen that the model fractures a bit earlier that the experiment, the damage model slightly underpredicts the total displacement at failure.

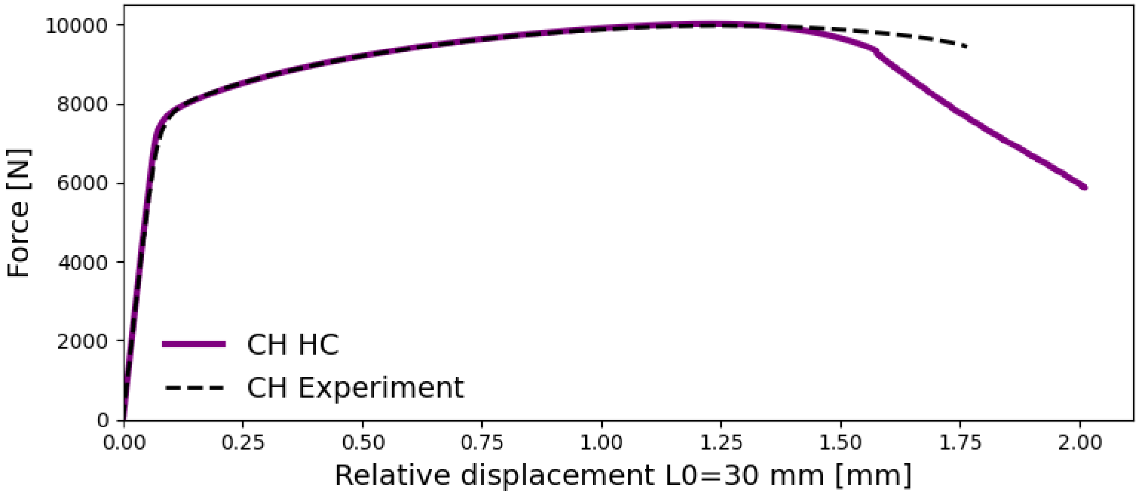

Figure 6.4: Force-displacement response of CH specimen

The simulated response of the CH specimen, depicted in Figure 6.4, behaves in a similar manner as the UT specimen. All material models exhibit a good agreement until the UTS point, beyond which they start to diverge. The biggest difference is seen in the 90° orientation.

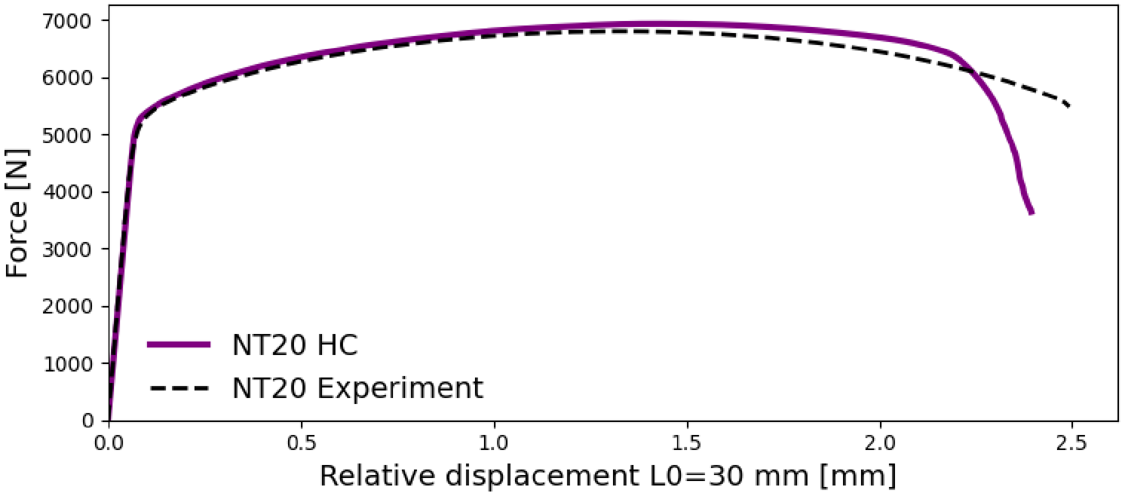

Figure 6.5: Force-displacement response of NT20 specimen

The simulated NT20 specimen shown in the Figure 6.5 shows a slight mismatch between the model and the experiment, since the material has only isotropic properties if fails to follow the experimetal force-displacement curve after the UTS point. The same behaviour was observed and commented in the previous chapter. The damage model underpredicts the total displacement at failure.

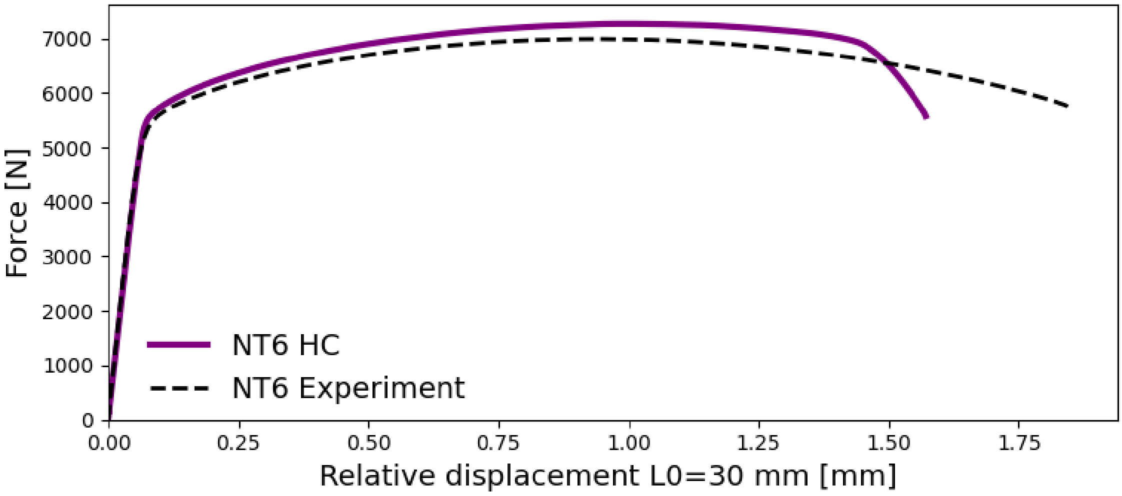

Figure 6.6: Force-displacement response of NT6 specimen

The simulated NT20 specimen shown in the Figure 6.5 shows a greater mismatch between the model and the experiment, the models underprecits the displacement at failure by about 1 mm.

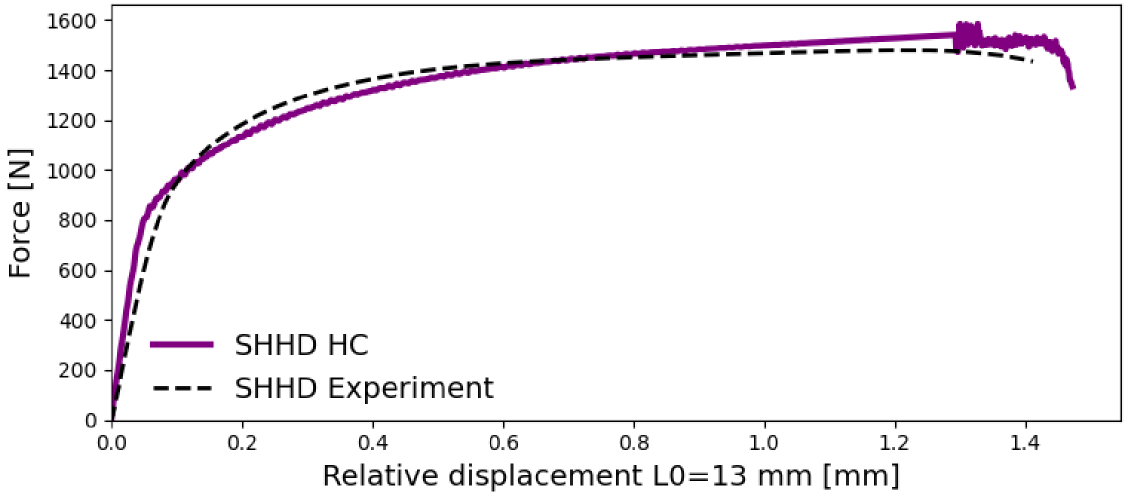

Figure 6.7: Force-displacement response of SHHD specimen

The simulated SHHD specimen shown in Figure 6.7 exhibits excellent agreement with the experimental data. At the moment of fracture some noise is present in the simulation but it doesn't affect the final result.

The initial calibration of the HC fracture surface gives satisfactory results. This fast calibration is was assumed that the stress triaxiality remained constant during loading. To fully calibrate the fracture surface an additional loop is needed. This iteration would involve defining the loading path to fracture and the relationship between the evolution of equivalent plastic strain and the stress triaxiality.

7 Conclusion

In this paper, the numerical model of the behaviour of the aluminium alloy 6014-T6 is presented, covering the entire range from the beginning of loading until fracture. The accuracy of numerical models is validated by experimental results. Experimental measurements are conducted on numerous samples of eight specimen types.
The paper provides a general overview of the use of aluminium alloys automotive industry, and the 6014-T6 aluminium alloy is presented. The paper outlines the theoretical description of the used combined Swift-Voce hardening law. Additionally, it provides a theoretical overview of the used anisotropic yield laws, including the Hill 48 and Barlat Yld2000 yield laws. The theoretical background of ductile damage is described, and the used Hosford-Coulomb ductile damage models is briefly explained. The paper provides the developed workflow for all the aforementioned laws and models. All the experimental testing was performed by the ETH Zurich University. The digital image correlation was conducted in *VIC-2D* software, the DIC method was used to obtain the displacement and strain field during loading. The tested specimen types geometries were chosen to cover the triaxiality area from the shear to the bi-axial stress state. Three shear specimen geometry types were tested, but due to the similar force-displacement response only one type was used for the numerical comparison. Numerical simulations were conducted in *Abaqus/Explicit* software, with the use of the *ANSA* pre-processor software.
The thesis was divided into three major tasks, the fist task was the calibration of the plastic hardening model, the second task was the calibration of two anisotropic models, the third task was the calibration of the damage model. The whole process was carefully documented, significant effort was dedicated to writing *Python* scripts for pre-processing

and post-processing of data.

The parameters of the combined Swift-Voce flow law were obtained from a least-square fit of stress-strain points using the *Python* software. From the force-displacement response it can be concluded that the proposed model very accurately describes the 6014-T6 hardening. The greatest accuracy is achieved for the uniaxial stress state. However, due to the anisotropy of extruded material, NT20 and NT6 specimens predictions exhibit non-negligible deviation from experimental results. Due to the anisotropy of extruded material, the mechanical properties in the non-extrusion direction are weaker. Due to specific geometry, the stress values are high in non-extrusion direction for these specimen types. The proposed Swift-Voce model uses the von Mises yield surface in combination with isotropic hardening, it can not adequately capture these effects.

The parameters of the Hill 48 and Barlat yield law are obtained from a least-square fit of stress and Lankford ratio points using the *Python* software. From the force-displacement response, it can be concluded that both of the proposed models very accurately describes the 6014-T6 anisotropic properties. Based on the available data, it can not be determined which model would be more suitable. However, literature suggests that REF is better suited for steel alloys.

The parameters of the Hosford-Coulomb ductile damage model are obtained from a least-square fit of total strain values before failure using the *Python* software. The calibration of damage model is a complex and time-consuming task, it this thesis a fast calibration was pursued with acceptable results. However, to achieve a more precise calibration of the fracture surface, it is necessary to preform an additional loop that considers the loading path to fracture.

Literature

[1] European Foundry Association et al. Aluminium in cars: Unlocking the lightweighting potential, 2013.

[2] Watch prozine. A post on porsche 911s. *Watch prozine*, 2020.

[3] Porsche Newsroom. The body of the taycan: Lightweight, safe, and innovative. *Porsche Newsroom*, 2020.

[4] Porsche Newsroom. The battery: Sophisticated thermal management, 800-volt system voltage. *Porsche Newsroom*, 2020.

[5] James K Wessel. *The handbook of advanced materials: enabling new designs*. Wiley Online Library, 2004.

[6] G.W.Birdsall. *Aluminium Heat Treating*. Reynolds Metals Company, 1958.

[7] Jessica Papasidero, Véronique Doquet, and Dirk Mohr. Ductile fracture of aluminum 2024-t351 under proportional and non-proportional multi-axial loading: Bao–wierzbicki results revisited. *International Journal of Solids and Structures*, 69:459–474, 2015.

[8] Von mises yield criterion — Wikipedia, the free encyclopedia, 2023. [Online; accessed 20-April-2023].

[9] Sharlin Shahid and Widaad Gukhool. Experimental testing and materialmodeling of anisotropy in injectionmoulded polymer materials, 2020.

[10] Keunhwan Pack, Thomas Tancogne-Dejean, Maysam B Gorji, and Dirk Mohr. Hosford-coulomb ductile failure model for shell elements: Experimental identification and validation for dp980 steel and aluminum 6016-t4. *International Journal of Solids and Structures*, 151:214–232, 2018.

[11] Thomas Pardoen and JW Hutchinson. An extended model for void growth and coalescence. *Journal of the Mechanics and Physics of Solids*, 48(12):2467–2512, 2000.

[12] Dirk Mohr and Stephane J Marcadet. Micromechanically-motivated phenomenological hosford–coulomb model for predicting ductile fracture initiation at low stress triaxialities. *International Journal of Solids and Structures*, 67:40–55, 2015.

[13] A Sancho, MJ Cox, T Cartwright, GD Aldrich-Smith, PA Hooper, CM Davies, and JP Dear. Experimental techniques for ductile damage characterisation. *Procedia Structural Integrity*, 2:966–973, 2016.

[14] Sung-Ju Park, Kangsu Lee, Burak Can Cerik, and Joonmo Choung. Comparative study on various ductile fracture models for marine structural steel eh36. *Journal of Ocean Engineering and Technology*, 33(3):259–271, 2019.

[15] Christian C Roth and Dirk Mohr. Ductile fracture experiments with locally proportional loading histories. *International Journal of Plasticity*, 79:328–354, 2016.

[16] Christian C Roth and Dirk Mohr. Determining the strain to fracture for simple shear for a wide range of sheet metals. *International Journal of Mechanical Sciences*, 149:224–240, 2018.

[17] Axel Klawonn, Martin Lanser, Oliver Rheinbach, and Matthias Uran. Fully-coupled micro–macro finite element simulations of the nakajima test using parallel computational homogenization. *Computational Mechanics*, 68(5):1153–1178, 2021.

[18] Omkar Kulkarni and Ganesh Kakandikar. Novel product design of tool for investigating formability with microstructural study of bio-material titanium grade-ii thin foils. *International Journal on Interactive Design and Manufacturing (IJIDeM)*, pages 1–11, 2022.

[19] Matej Stanić. *Calibration and validation of a damage model for 6005-T6 aluminium.* PhD thesis, University of Zagreb. Faculty of Mechanical Engineering and Naval Architecture, 2021.

[20] DS Dassault Systèmes. Abaqus analysis user's guide. *Abaqus Documentation, Simulia Corp., Waltham, MA, Report*, 2016.